

## Chapter 7

# Orientation Imaging Microscopy and Grain Boundary Analysis in Tempered Power Plant Steel

Over the past decade, the rapid, automated acquisition of large numbers of grain orientation data in the SEM has become possible. The sampling volume for each measurement is sufficiently small that many measurements can be made within a single grain, enabling point-by-point ‘maps’ of orientation data to be obtained and related directly to microstructure. By comparing data from adjacent points, it is also possible to determine the positions and characteristics of grain boundaries.

Using this technique, grain orientations and grain boundaries in  $2\frac{1}{4}\text{Cr1Mo}$  steels in the as-quenched and tempered states were investigated, giving a more complete microstructural characterisation than would be possible by conventional optical microscopy and SEM. The purpose of the study was to obtain insight into the likely microstructural origins of the changes in the Barkhausen noise signal with tempering.

## 7.1 Grain orientation

The specification of grain orientations requires the definition of a crystal coordinate system  $\mathbf{c}_c$ , which is usually chosen with reference to the crystal symmetry, and a sample system  $\mathbf{c}_s$ . This may be based on rolling, transverse and normal directions if these exist, but is otherwise defined arbitrarily. The crystal orientation is defined by the rotation matrix  $\mathbf{G}$  which brings the crystal system into coincidence with the sample system.

$$\mathbf{c}_c = \mathbf{G} \cdot \mathbf{c}_s \quad (7.1)$$

The elements of  $\mathbf{G}$  are given by:

$$\mathbf{G} = \begin{pmatrix} \cos \alpha_1 & \cos \beta_1 & \cos \gamma_1 \\ \cos \alpha_2 & \cos \beta_2 & \cos \gamma_2 \\ \cos \alpha_3 & \cos \beta_3 & \cos \gamma_3 \end{pmatrix} \quad (7.2)$$

where  $\alpha_1$ ,  $\beta_1$  and  $\gamma_1$  are the angles between the crystal axis [100] and the specimen axes  $X$ ,  $Y$  and  $Z$  respectively and the second and third rows of cosines correspond to the [010] and [001] axes referred to the same sample axes.

Only three independent variables are required to specify a crystal orientation, so the matrix format contains a certain amount of redundant information. A variety of methods have been developed to represent orientation information more succinctly. These include pole figures, inverse pole figures, Euler angles and angle-axis pairs.

### 7.1.1 Pole figures and inverse pole figures

If a crystal is envisaged at the centre of a sphere, a crystal axis can be described by the point, or pole, at which it intersects the sphere surface. In two dimensions, the stereographic projection of the sphere and the poles, projected with reference to specified sample axes, form a pole figure. An indication of the sample texture can be obtained by plotting the poles of selected crystal axes from a large number of crystals.

If, instead, directions in the sample coordinate system are projected onto the crystal coordinates, the result is an inverse pole figure. Because of crystal symmetry, a single stereographic triangle contains all necessary information. In materials with cubic symmetry, the triangle containing  $\langle 100 \rangle$ ,  $\langle 110 \rangle$  and  $\langle 111 \rangle$  is used.

### 7.1.2 Euler angles

The three Euler angles are the angles of rotations which are applied sequentially to bring the sample coordinate system into coincidence with the crystal system. Several alternative conventions for these exist but the Bunge system (Bunge, 1965, 1985) is the most commonly used, and is the system used by the automated orientation analysis software described below.

### 7.1.3 Angle-axis pairs

Orientations can be described as a single rotation performed about a specified axis to map the crystal coordinates onto the sample coordinates. This notation can be used to describe differences in orientation between adjacent grains (misorientations) as well as the orientations of individual crystals.

The matrix of misorientation  $\mathbf{M}$  between grains of orientations  $\mathbf{G}_1$  and  $\mathbf{G}_2$  is calculated from:

$$\mathbf{M}_{12} = \mathbf{G}_1^{-1}\mathbf{G}_2 \quad (7.3)$$

where one of the grains is arbitrarily designated as the reference grain, with orientation  $\mathbf{G}_1$ . The misorientation angle-axis pair,  $\theta\langle UVW \rangle$ , where  $U^2 + V^2 + W^2 = 1$ , and  $\theta$  is measured in a right-handed sense, is obtained from  $\mathbf{M}$  using the equations:

$$\cos \theta = (M_{11} + M_{22} + M_{33} - 1)/2 \quad (7.4)$$

$$\begin{aligned} U &= M_{23} - M_{32} \\ V &= M_{31} - M_{13} \\ W &= M_{12} - M_{21} \end{aligned} \quad (7.5)$$

(Santoro and Mighell, 1973).

The angle-axis pair description is commonly used to describe grain misorientations because it can be related to the geometry of the grain boundary separating adjacent grains.

## 7.2 Grain boundary geometry

A grain boundary is the plane where two crystals of different orientations meet. Figure 7.1 shows an imaginary extension of the lattices of two crystals so that they interpenetrate with a common origin. The misorientation angle-axis pair  $\theta < UVW >$  describes the rotation which must be performed to bring Lattice 1 into coincidence with Lattice 2. A possible grain boundary plane is marked on the left-hand diagram, but the position of this is not defined by  $\theta < UVW >$ . A parameter characterising the grain boundary plane normal is required for a complete macroscopic characterisation of the boundary.

The left-hand diagram is a special case of grain boundary in which  $< UVW >$  lies in the grain boundary plane. This is known as a tilt boundary. A general boundary consists of a tilt component and also a twist component (a component of  $< UVW >$  perpendicular to the boundary plane); an example of such a boundary is shown in the right-hand diagram.

The imaginary interpenetrating region in Figure 7.1 contains lattice points from both crystal lattices. Certain rotations  $\theta < UVW >$  will cause some of the lattice points from Lattice 1 to come into coincidence with Lattice 2 points, giving a superlattice of coincident points. This is known as a coincidence site lattice (CSL) and has already been mentioned briefly in Chapter 3. CSLs are characterised by a parameter  $\Sigma$ , which is the reciprocal of the ratio [ number of lattice points in coincidence: total number of lattice points]. A  $\Sigma 3$  CSL is thus one in which 1 in 3 lattice points are coincident sites.

### 7.2.1 The coincidence site lattice model

The CSL is a fictitious concept, since the two lattices do not really interpenetrate, but it has relevance at the grain boundary, where they meet. A CSL

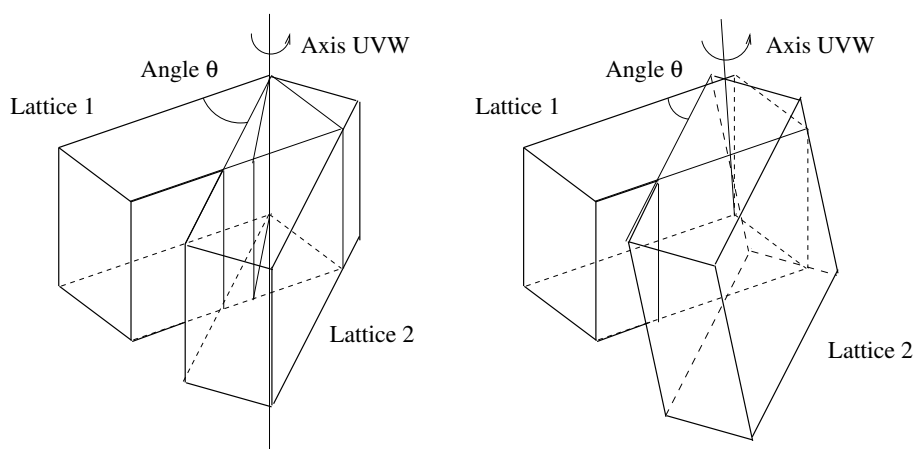


Figure 7.1: The angle-axis pair  $\theta \langle UVW \rangle$  characterises the crystallographic orientation between the two grains but the actual boundary can be anywhere. After Randle and Engler, 2000.

model of grain boundary geometry was proposed by Kronberg and Wilson (1949) and extended by Brandon *et al.* (1964) and Brandon (1966). The number of coincidence sites present on the grain boundary plane depends on the orientation of the plane, as well as the relationship between the two lattices. Planes with a higher proportion of coincidence sites allow better matching and a closer fit than those with few or no such sites, and this special periodicity has been linked with superior materials performance in many applications (*e.g.* Watanabe, 1993, Randle, 1996). Since the existence of a coincidence boundary requires precise angle and axis values, it might be expected that such boundaries would be too rare to be of relevance in general. However, it has been found that boundaries whose angle-axis pairs are close to those for true coincidence can also exhibit special properties. In such cases, the periodicity at the lattice is conserved by the introduction of grain boundary dislocations (Bollmann, 1970). This is similar to the description of low-angle boundaries, of misorientation  $10\text{--}15^\circ$  or less, as periodic arrays of dislocations (Read and Shockley, 1950). Low-angle boundaries are included in the CSL model as a special case,  $\Sigma 1$ , in which all lattice sites coincide in the ideal geometry.

The Brandon criterion, giving the maximum allowable deviation  $\nu_m$  from

ideal coincidence for a  $\Sigma$  coincidence boundary, is:

$$\nu_m = \nu_0 \Sigma^{-1/2} \quad (7.6)$$

where  $\nu_0$  is a constant of proportionality set to  $15^\circ$ , the maximum allowable deviation for a low-angle ( $\Sigma 1$ ) boundary. Thus, boundaries with smaller  $\Sigma$  accommodate a greater possible deviation. This criterion is almost universally used for the categorisation of grain boundaries (Randle, 1993). The Brandon ratio, characterising the deviation from coincidence, is the actual misorientation normalised by  $\nu_m$  for that value of  $\Sigma$ . When assessing grain boundary types, the  $\Sigma$  for which the Brandon ratio is smallest is chosen. Boundaries which do not fulfil the criterion for any CSL are designated as random.

The  $60^\circ \langle 111 \rangle$ ,  $\Sigma 3$  boundary type is of particular interest. If the boundary plane is either  $\{111\}$  or  $\{211\}$  as referred to the crystal lattice, this is a twin boundary, in which all the sites in the plane are coincidence sites. Most other low- $\Sigma$  CSL boundaries also exhibit twinning on certain planes, but it is the  $60^\circ \langle 111 \rangle$  orientation which is most commonly referred to as a ‘twin’ orientation in the literature (Randle, 1993).

### 7.2.2 Estimation of grain boundary energy

Grain boundaries have an intrinsic energy over and above that of the crystal lattice. As reported by Randle (1996), grain boundary energies tend usually to correlate with the free volume at the boundary. The periodicity in CSL arrangements reduces the free volume compared to random boundaries and thus a lower energy is expected. Determination of the misorientation dependence of boundary energies, by calculation or experiment, have mainly been performed on high-symmetry boundaries in pure metals (*e.g.* Tsurekawa *et al.*, 1994; Nakashima and Takeuchi, 2000). General boundaries in alloys are likely to have much higher energy (Randle, 1996). Extrinsic influences on grain boundary energy include precipitates, lattice dislocations, vacancies and impurity atoms, all of which tend to segregate to boundaries because of the increased free volume. It is not, therefore, possible to estimate grain

boundary energies in the  $2\frac{1}{4}\text{Cr1Mo}$  steels in this study based only on misorientation measurements.

## 7.3 Electron Backscatter Diffraction

The development of SEM-based electron backscatter diffraction (EBSD) techniques dates back to the 1970s (Venables and Harland, 1973; Venables and bin-Jaya, 1977) although backscatter patterns had, in fact, been observed earlier than this (Blackham *et al.*, 1953).

When the SEM is configured to give a focused spot of electrons on one point of the sample rather than a scanning beam, diffraction occurs by the elastic scattering of incident electrons in all directions. A plane wave hitting an isolated atom causes the emission of spherical waves of the same wavelength. If the atom is in a crystal lattice, most of these spherical waves will interfere destructively, but at certain angles they will be in phase. These angles were shown by Bragg (1913) to be related to the interplanar spacing  $d$  of the crystal lattice:

$$n\lambda = 2d \sin \theta_B \quad (7.7)$$

where  $n$  is an integer,  $\lambda$  is the wavelength of the radiation and  $\theta_B$  is the Bragg angle corresponding to diffraction from planes of spacing  $d$ .

### 7.3.1 Formation of Kikuchi patterns

Since the backscattered electrons are scattered in all directions, some will be at the correct Bragg angle  $\theta_B$  for diffraction from each of the crystal planes in the lattice. Diffraction occurs in all directions, resulting in Kossel cones of diffracted radiation, whose half-apex angle is  $90^\circ - \theta_B$  (Figure 7.2). In electron diffraction, for typical values of the electron wavelength, the Bragg angles are around  $0.5^\circ$ , giving cone apex angles of nearly  $180^\circ$ ; the cones therefore appear almost flat. Each set of crystal planes produces two cones, which can be considered as emanating from a source between parallel planes, with one cone from the upper and one from the lower side of the source.

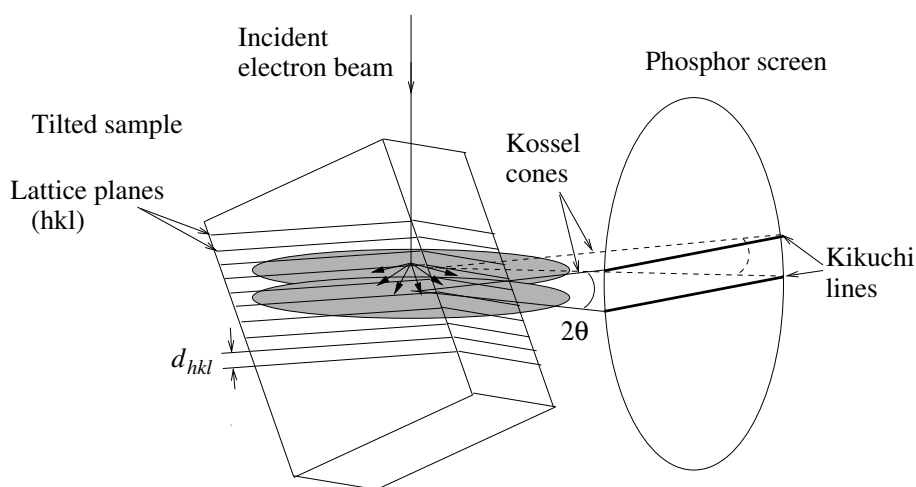


Figure 7.2: Geometry of electron backscatter diffraction; after Randle and Engler, 2000.

When the cones intersect a flat plate such as a phosphor screen, they appear almost as pairs of parallel lines (Kikuchi lines). The Kikuchi pattern is a gnomonic projection of relationships within the crystal (Figure 7.3). If the crystal is envisaged at the centre O of a sphere of radius  $r$ , and the phosphor screen is a tangent plane to the sphere at position N, a direction in the crystal is projected as a pole P. Each pair of lines has a characteristic spacing corresponding to the set of planes from which it originates. The points of intersection of Kikuchi bands represent major zone axes in the crystal.

### 7.3.2 Indexing Kikuchi patterns

Extraction of orientation information from Kikuchi patterns is possible for an experienced user, but over the last decade, an automated system has been developed and demonstrated to be as accurate as manual indexing and many times faster (Adams *et al.*, 1993; Wright, 1993). An algorithm known as the Hough transform is used to recognise the edges of the Kikuchi bands (Wright, 1993). This consists of applying to each pixel the equation:

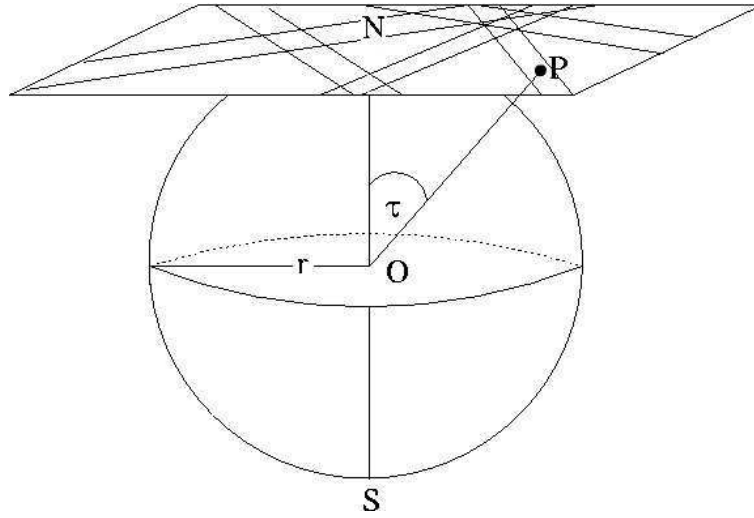


Figure 7.3: The Kikuchi diffraction pattern as a gnomonic projection of angles within the crystal; after Randle and Engler, 2000.

$$\rho_i = x_k \cos \theta_i + y_k \sin \theta_i \quad (7.8)$$

where  $(x_k, y_k)$  are the coordinates of a pixel in the original image and  $(\rho_i, \theta_i)$  are the parameters of a straight line passing through  $(x_k, y_k)$ . The sinusoidal curves generated by collinear points intersect at a single point, whose values of  $\rho$  and  $\theta$  characterise the line, as described by Krieger Lassen (1996).

For correct indexing, the crystal system, chemical composition, unit cell dimensions and atomic positions of the material must be supplied to the analysis software. A background image is obtained from a large area while the microscope is in scanning mode, stored, and subtracted from the backscatter pattern obtained at every point to ensure that the contrast investigated by the software comes only from the EBSD pattern. Before the system is used, the specimen-to-screen distance and position of the pattern centre are obtained by calibration. An early calibration method is described by Venables and bin-Jaya (1977) and several modern methods by Randle and Engler (2000). When calibrated correctly, an EBSD system can calculate grain misorientations to an accuracy of  $\pm 0.5^\circ$  (Dingley and Randle, 1992).

### 7.3.3 Diffraction geometry in the SEM

Figure 7.4 shows the arrangement of the hardware for automated electron backscatter diffraction. The sample is tilted through an angle of  $70^\circ$  to the horizontal to reduce the path length of backscattered electrons and allow more electrons to escape from the surface and be detected (Venables and Harland, 1973). It lies in the eucentric plane, enabling it to remain in focus when the stage is moved in the surface plane, and is mounted on a piezoelectric stage capable of motions of  $0.1 \mu\text{m}$ . Modern systems use a forward-mounted backscatter detector (the phosphor screen in Figure 7.4) and a camera to record diffraction patterns (Randle and Engler, 2000).

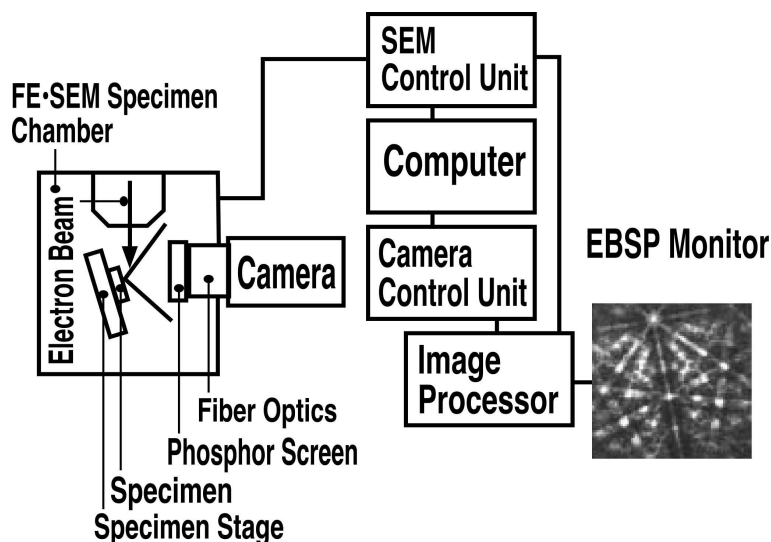


Figure 7.4: Experimental setup for SEM-based EBSD at Tohoku University. Diagram by K. Kawahara; used with permission.

## 7.4 Automated Orientation Imaging Microscopy

The development of automated Kikuchi pattern indexing led to the new technique of Orientation Imaging Microscopy (OIM). Television-based systems for capturing backscatter patterns and computer systems able both to

control the stage or electron beam position and to index patterns with minimal or no human intervention were developed (Adams *et al.*, 1993; Wright *et al.*, 1993). This allows the rapid acquisition of a large number of orientation data. Current systems are able to solve a Kikuchi pattern in less than one second using a standard PC (Randle and Engler, 2000).

The user typically programs in an array of positions from which orientation data should be acquired by specifying the spatial range and step size of sampling points. A hexagonal or square grid can be chosen but hexagonal tends to be preferred since each hexagon has six nearest neighbours, while in a square grid, four nearest and four next-nearest neighbours must be considered (Randle and Engler, 2000). A single data point is obtained as follows: the stage is moved to a specified point, the camera captures the Kikuchi pattern, and this is analysed and the Euler angles, stage position and image quality (§ 7.4.2) are recorded (Wright, 1993).

## 7.4.1 Representation of data

### Orientation mapping

Automated OIM allows maps of the spatial dependence of orientation data to be plotted and related directly to microstructural features. Colour can be used to represent particular orientations or texture components (Wright, 1993). OIM observations have demonstrated that variations in orientation can occur within a single grain, making the definition of concepts such as grain size less definite than was previously believed (Adams *et al.*, 1993). In addition, boundaries were apparent which could not be seen on a conventional SEM image of the same area.

At grain boundaries, the Kikuchi patterns from neighbouring grains may overlap, producing a complex pattern which cannot be solved correctly by the indexing system (Adams *et al.*, 1993). Various ‘clean-up’ algorithms are available in the computer software to assign orientation values to such indeterminate points. The criteria used for this operation by the algorithms are described in detail in the software documentation, supplied by Tex-SEM Ltd. The clean-up process does alter the data set and should not be used

carelessly since it may introduce spurious features.

### Grain boundary properties

Using the orientation data from neighbouring points, it is possible to determine the positions and misorientation angles of grain boundaries (Wright, 1993). Currently available software can identify coincidence boundaries and produce a colour-coded map according to  $\Sigma$ . Adams *et al.* (1993) noted that some of the boundaries identified appeared to terminate in grain interiors. Since this is topographically impossible, it was attributed to differences in orientation along the boundaries which, in some positions, cause the measured misorientation to fall below the arbitrarily designated minimum misorientation required to identify a grain boundary. OIM analysis is only two-dimensional and does not give information on the grain boundary plane orientation, but serial sectioning techniques have been developed to study this (Wall *et al.*, 2001).

### Statistical approaches

The large numbers of data acquired using OIM allow statistical analyses of, for example, the distribution of misorientation angles  $\theta$  between pairs of sampling points (Wright, 1993). This can be compared with theoretical predictions assuming a random distribution or a particular orientation relationship.

#### 7.4.2 Image Quality

The image quality (IQ) of Kikuchi patterns, as represented by the sharpness of the lines, has been quantified and related to the level of deformation present in specimens (Quested *et al.*, 1988; Wilkinson and Dingley, 1991). The quantification method in current use was proposed by Krieger Lassen *et al.* (1994) and gives IQ values between 0 and 1, where 0 represents the worst image quality (no definition at all) and 1 the best. Since the development of automated OIM, image quality measurements can be obtained at every sampling point and displayed as a map. Minimum-quality points were

found to coincide with grain boundaries (Adams *et al.*, 1993; Wright, 1993) but could also be present in certain areas within grain interiors. This was attributed to high dislocation density. Image qualities were higher in certain grains than in others.

As well as the deformation state, IQ depends on the accelerating voltage, beam current, the state of the vacuum, the filament quality and alignment, and the specimen preparation (Randle and Engler, 2000). It may also depend on orientation but this has not yet been investigated fully. IQ measurements are not, therefore, fully quantitative, but semi-quantitative comparisons can be made within a single scan, enabling heavily deformed regions to be identified.

## 7.5 OIM observations of martensitic steels

### 7.5.1 Crystallographic relationships

A martensitic packet identified by optical microscopy or conventional SEM as a region of parallel laths is designated a ‘morphological’ packet. By contrast, a ‘crystallographic’ packet is a region of uniform orientation as determined by EBSD. Gourgues *et al.* (2000) studied the relationship between the two packet types in a low-alloy steel. Crystallographic packets were found to be much smaller than morphological packets, and to correspond to the ‘blocks’ in Figure 2.4. Between neighbouring blocks of the same morphological packet, the misorientation angle-axis pairs were mostly  $60^\circ < 111 >$  but occasionally  $55^\circ < 110 >$ . This suggests that the blocks within a packet have a close-packed plane parallel to the same prior austenite prior austenite  $\{111\}$  plane and are mostly twin related. The misorientation angle distribution had a peak for  $\theta = 60^\circ$ . This was compared with theoretical distributions for Kurdjumov-Sachs and Nishiyama-Wasserman relationships, and it was concluded that Kurdjumov-Sachs corresponded more closely to the real data.

Previous TEM work had shown that each individual martensitic lath could nucleate with one of the six possible crystallographic variants from the same austenite  $< 111 >$  (Chilton *et al.*, 1970; Sarikaya *et al.*, 1986). However,

Gourgues *et al.* instead found that martensite formed blocks of many laths with the same orientation.

Low-angle boundaries were found within crystallographic packets (blocks). The internal structure of a packet consists of several slightly misoriented groups of laths. The misorientations are present because of the high dislocation density associated with the shear strain of transformation from austenite to martensite.

In a 9 wt. % Cr steel subjected to a short tempering treatment after quenching, crystallographic packet sizes increased slightly with increasing prior austenite grain size (Barcelo *et al.*, 2002). The pole figures of the  $\langle 200 \rangle$  axis from single prior austenite grains did not correspond directly to either the Kurdjumov-Sachs or the Nishiyama-Wasserman relationship although it showed some similarities to both. In small prior austenite grains ( $\sim 15 \mu\text{m}$ ), only a subset of the possible variants predicted by either relationship were observed, but larger grains ( $> 40 \mu\text{m}$ ) contained all the possible variants.

### 7.5.2 Creep-deformed martensitic steels

In martensitic 9Cr1Mo, 9Cr3Co and 9Cr3W3Co (wt. %) steels, the microstructure was very inhomogeneous, with some blocks extending to  $10 \mu\text{m}$  and others as small as  $1 \mu\text{m}$  (Nakashima *et al.*, 2000, 2001; Yoshida *et al.*, 2002). Areas of indeterminate orientation were present, but these were eliminated by creep deformation. They were attributed to high dislocation density, which is reduced by dynamic recovery during creep.

The misorientation angle distribution for boundaries with common axis  $\langle 110 \rangle$  was determined. In the 9Cr1Mo steel, peaks were found at low angles and in the regions around  $60^\circ$  and  $80^\circ$ . This agreed reasonably well with the values of  $10^\circ$ ,  $50.5^\circ$  and  $70.5^\circ$  predicted from the Kurdjumov-Sachs relationship. Peaks at similar positions were found in the 9Cr3Co and 9Cr3W3Co steels. Creep deformation of the 9Cr1Mo steel decreased the number of grain boundaries with a specific orientation relationship and increased the number of random boundaries.

## 7.6 Experimental technique

### 7.6.1 Sample Preparation

An AQ sample and samples tempered at 600°C for 4, 16, 64, 128 and 256 hours were selected for observation. They were prepared as described in § 6.1, but instead of the final polishing stage described there, they were polished to 6  $\mu\text{m}$  using diamond paste, and to 0.1  $\mu\text{m}$  using alumina slurry. They were then electropolished using a mixture of 164  $\text{cm}^3$  acetic acid, 18  $\text{cm}^3$  perchloric acid and 18  $\text{cm}^3$  methanol which was cooled in iced water and stirred during polishing. The polishing conditions were 20–30 V for 3–5 minutes, with adjustments made depending on the appearances of the surfaces.

### 7.6.2 Orientation Imaging Microscopy

A Hitachi S-4200 Field Emission Gun Scanning Electron Microscope (FEG-SEM), belonging to the Materials Design and Interface Engineering Laboratory at Tohoku University, was used for the observations. The OIM system is shown schematically in Figure 7.4.

The accelerating voltage was 30 kV, the beam current 50 pA, and the beam penetration depth several tens of nanometres. A large spot size was used to maximise the backscattered signal. Operation of the OIM system was controlled using purpose-designed software by Tex-SEM Ltd. The step size was set to 0.1  $\mu\text{m}$ , and the magnification to 6000 $\times$ , to allow investigation on the lath scale.

Before acquisition of each data set, EBSD patterns were obtained from points on the sample surface to check the image quality. If this was adequate, a 14 x 15  $\mu\text{m}$  area on the surface was selected and imaged using conventional SEM. After changing to backscatter mode, the scan was begun and left to run automatically. A complete scan took between two and three hours using this system.

Three scans were obtained from each of the steel samples at different positions on the surface. However, since the working distance between the pole piece and surface should be kept at approximately 15 mm for EBSD,

this only gave a limited range of regions for sampling.

## 7.7 Results

OIM maps and micrographs are presented in Figure 7.7–Figure 7.24. On each page, the top two diagrams are colour-coded maps of the orientation of the sample normal axis with respect to the crystal axes of the lattice. The colour key is given in Figure 7.5. The maps do not give comprehensive information, since there is a degree of freedom in rotation perpendicular to this direction, but it is possible to identify both gradual and abrupt orientation changes by their differences in colour.

The top left-hand diagram contains the raw orientation data, including indeterminate points, and the right-hand diagram is the result of a ‘clean-up’ algorithm, Grain Dilation. This takes an indeterminate point bordered by points belonging to grains, and assigns an orientation to it based on the orientations of its neighbours. (Full details of its operation are given in the software documentation.) The algorithm is iterative and operates until all points have been assigned to grains. The user is prompted to supply the minimum number of points which must be in a cluster if it is to be considered a grain; in this study, this was set at 4.

Beneath the raw data map is a grey-scale map of image quality. The lighter the colour, the higher the IQ. To the right of this is a grain boundary map calculated from the cleaned orientation data. These were used in preference to the raw data because most of the indeterminate points occurred at grain boundaries, obscuring the true orientation relationships between the grains. Figure 7.6 is the colour key for this map: red represents a low-angle boundary ( $2 \leq \theta < 15^\circ$ ), light green is  $\Sigma 3$ , black is random, and other colours are used to represent boundaries with different  $\Sigma$  values, as determined by the Brandon criterion. Misorientations of  $< 2^\circ$  between adjacent points are not considered to be grain boundaries.

The lowest image is a conventional SEM micrograph of the same area. The electropolishing removes much of the surface relief, so some of these images are of poor quality.

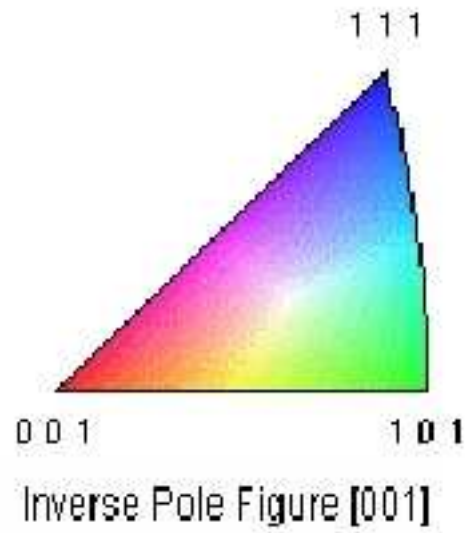


Figure 7.5: Colour-coded pole figure key for orientation maps. Colour corresponds to orientation of  $[100]$  specimen axis with respect to crystal axes  $[001]$ ,  $[111]$  and  $[101]$ .

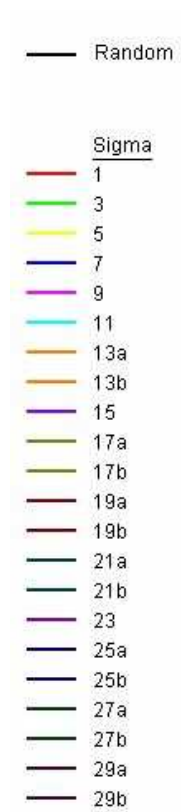


Figure 7.6: Key to grain boundary maps.

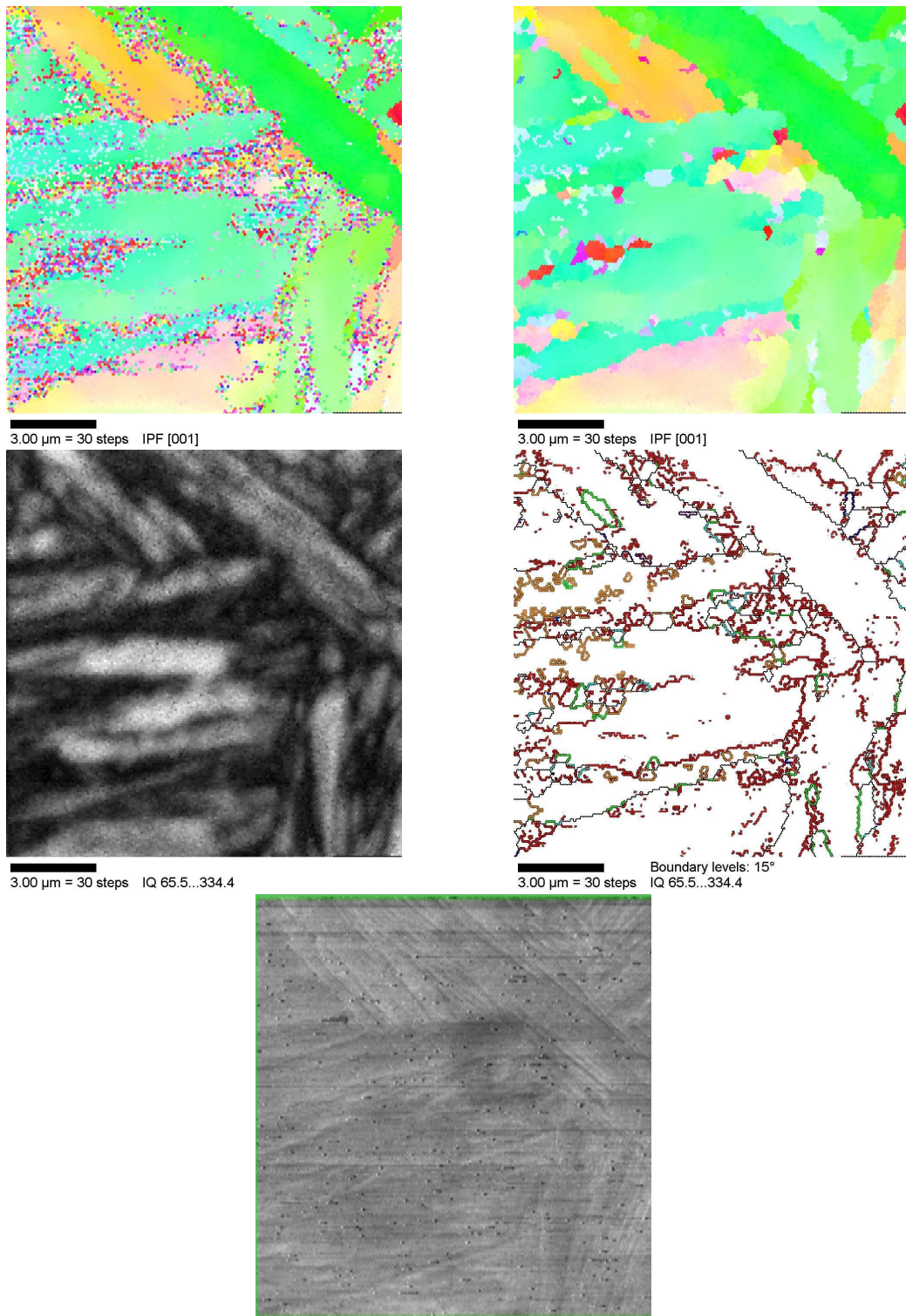


Figure 7.7:  $2\frac{1}{4}$ Cr1Mo steel, as-quenched

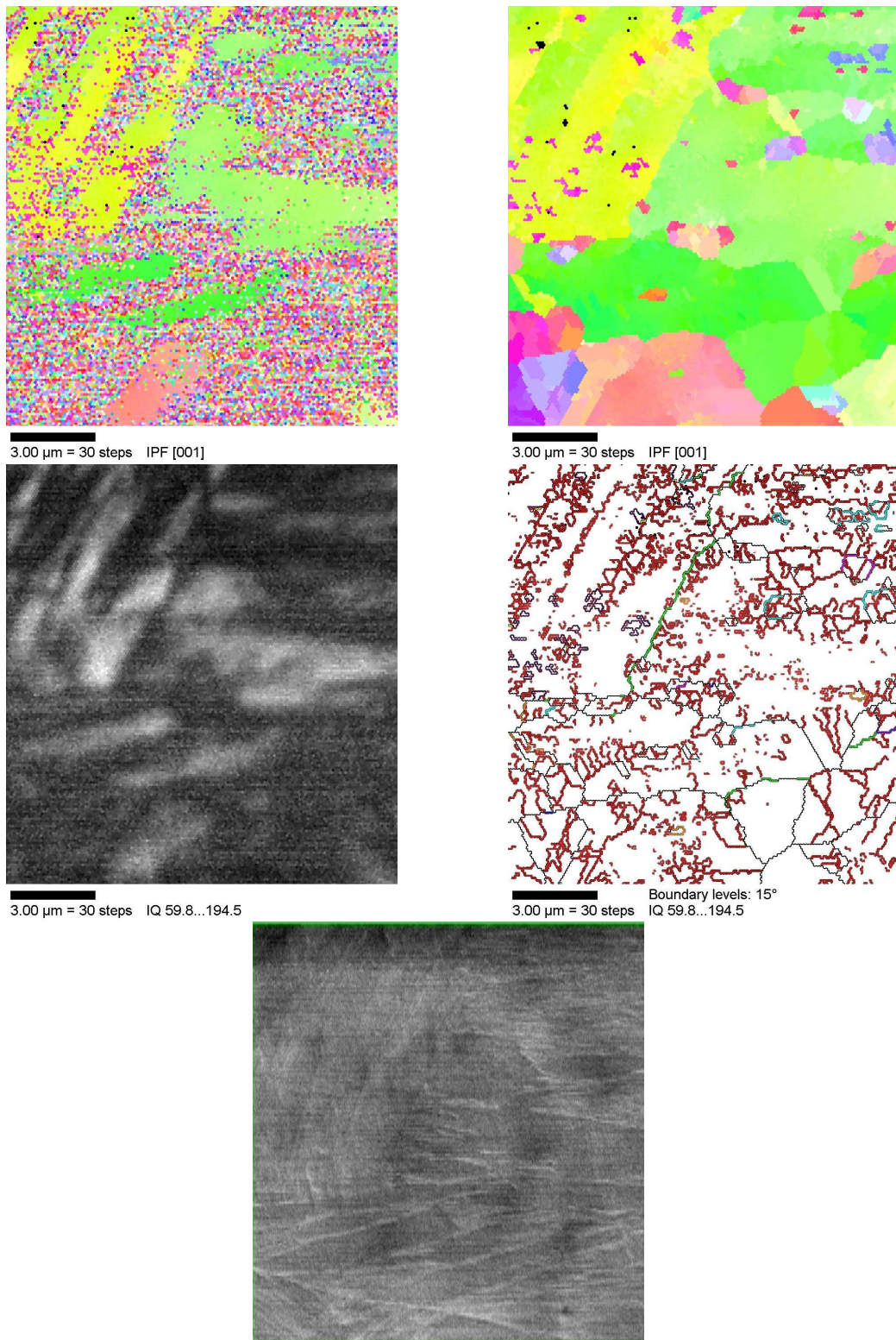


Figure 7.8:  $2\frac{1}{4}\text{Cr1Mo}$  steel, as-quenched

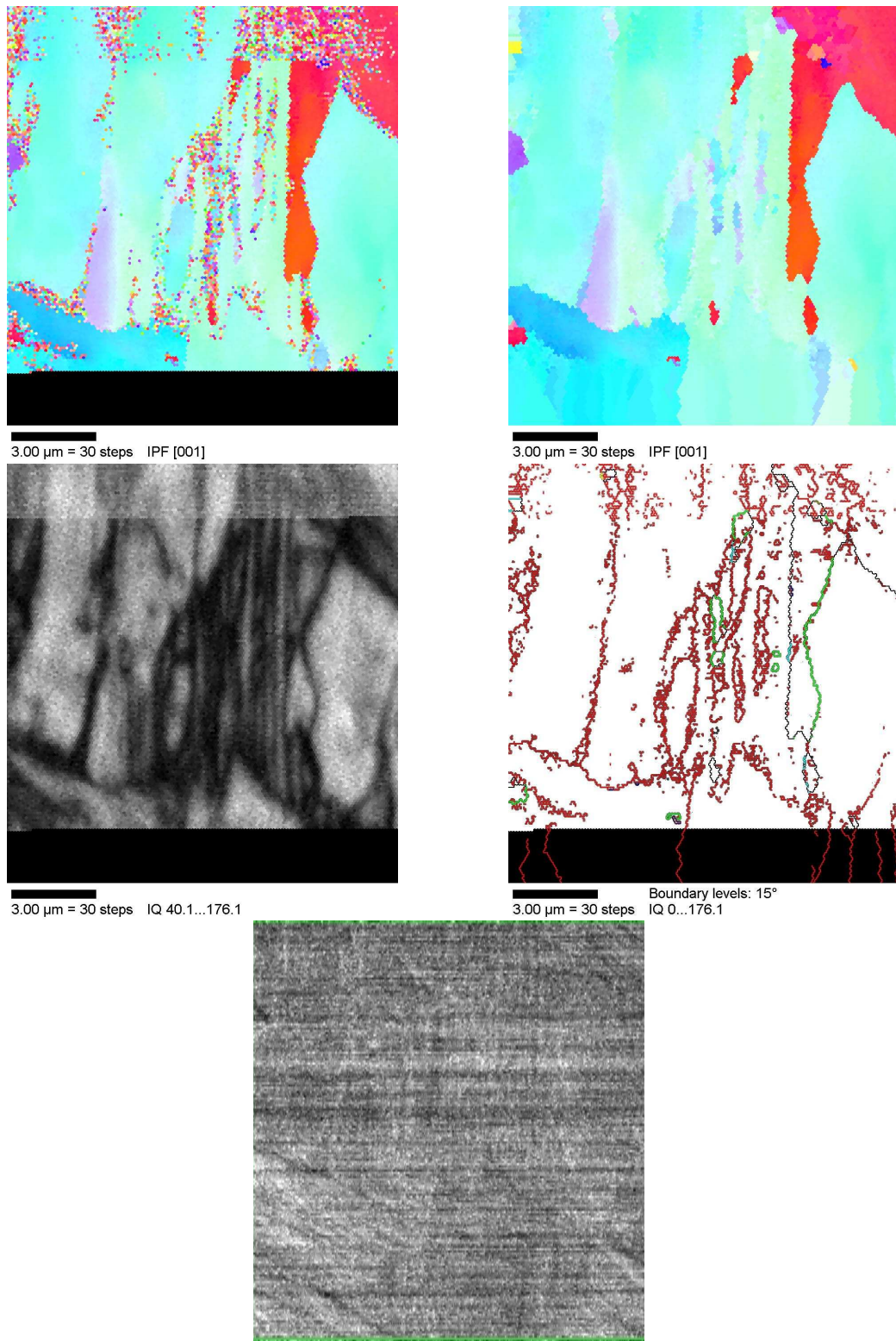


Figure 7.9:  $2\frac{1}{4}$ Cr1Mo steel, as-quenched  
- 174 -

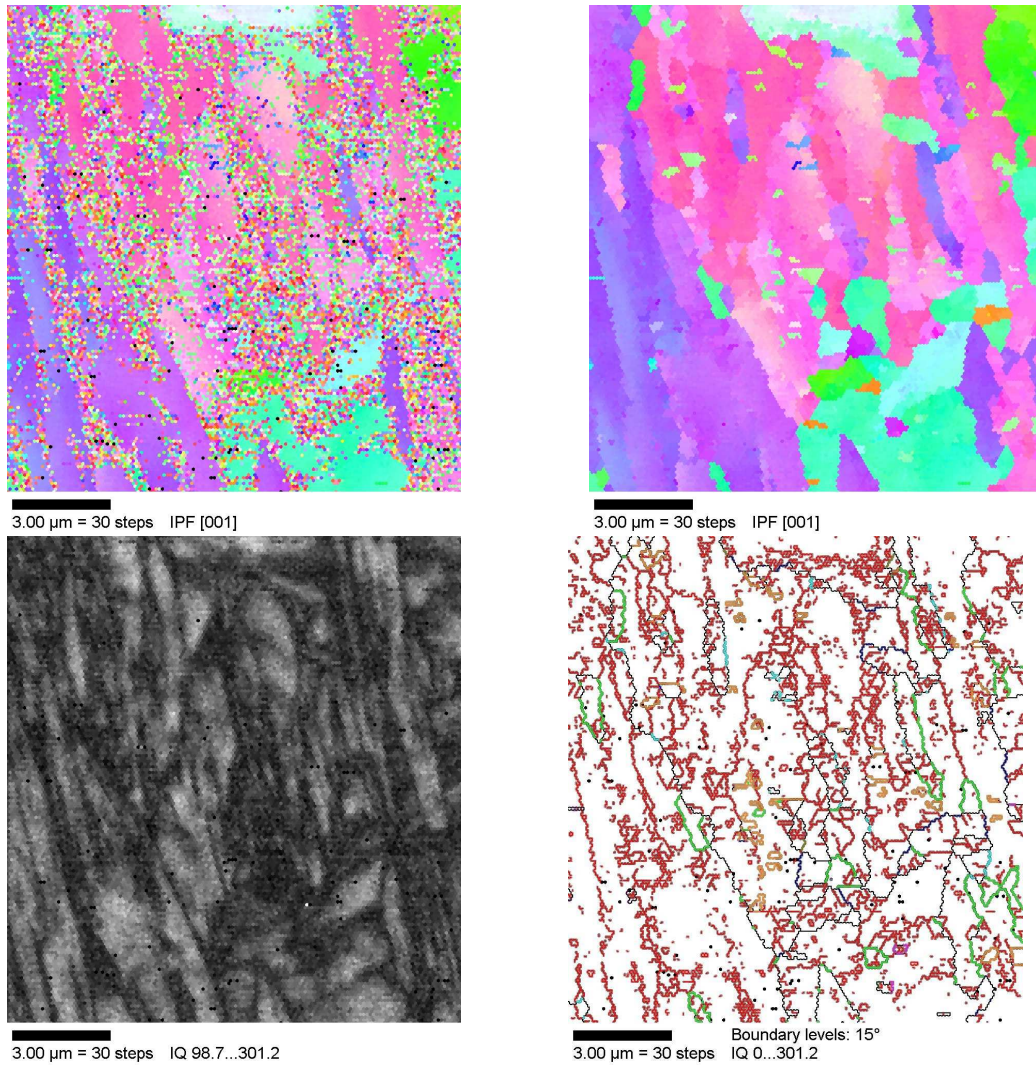


Figure 7.10:  $2\frac{1}{4}$ Cr1Mo steel, 600 °C, 4 hours tempering

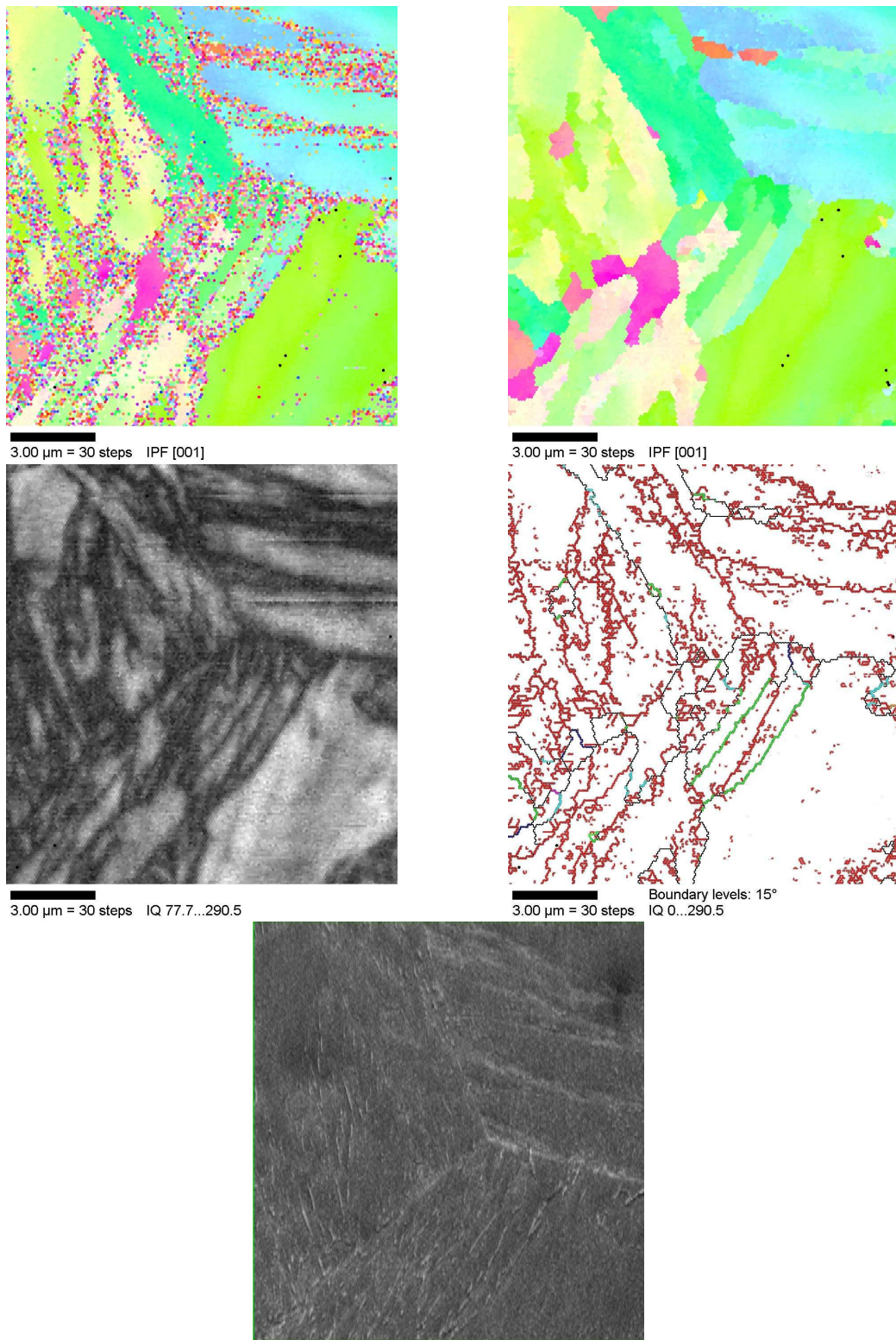


Figure 7.11: 2 $\frac{1}{4}$ Cr1Mo steel, 600 °C, 4 hours tempering

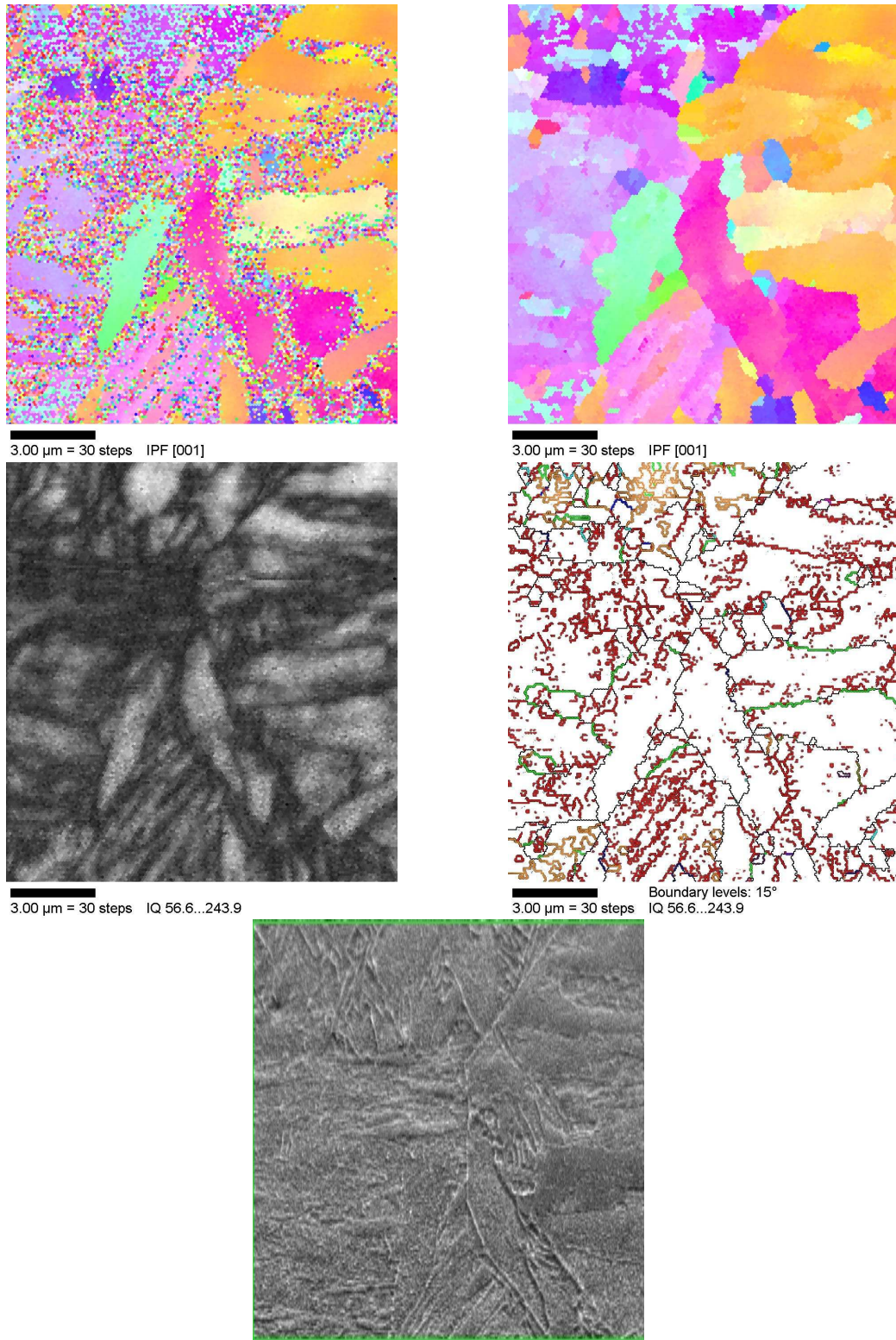


Figure 7.12:  $2\frac{1}{4}$ Cr1Mo steel, 600 °C, 4 hours tempering

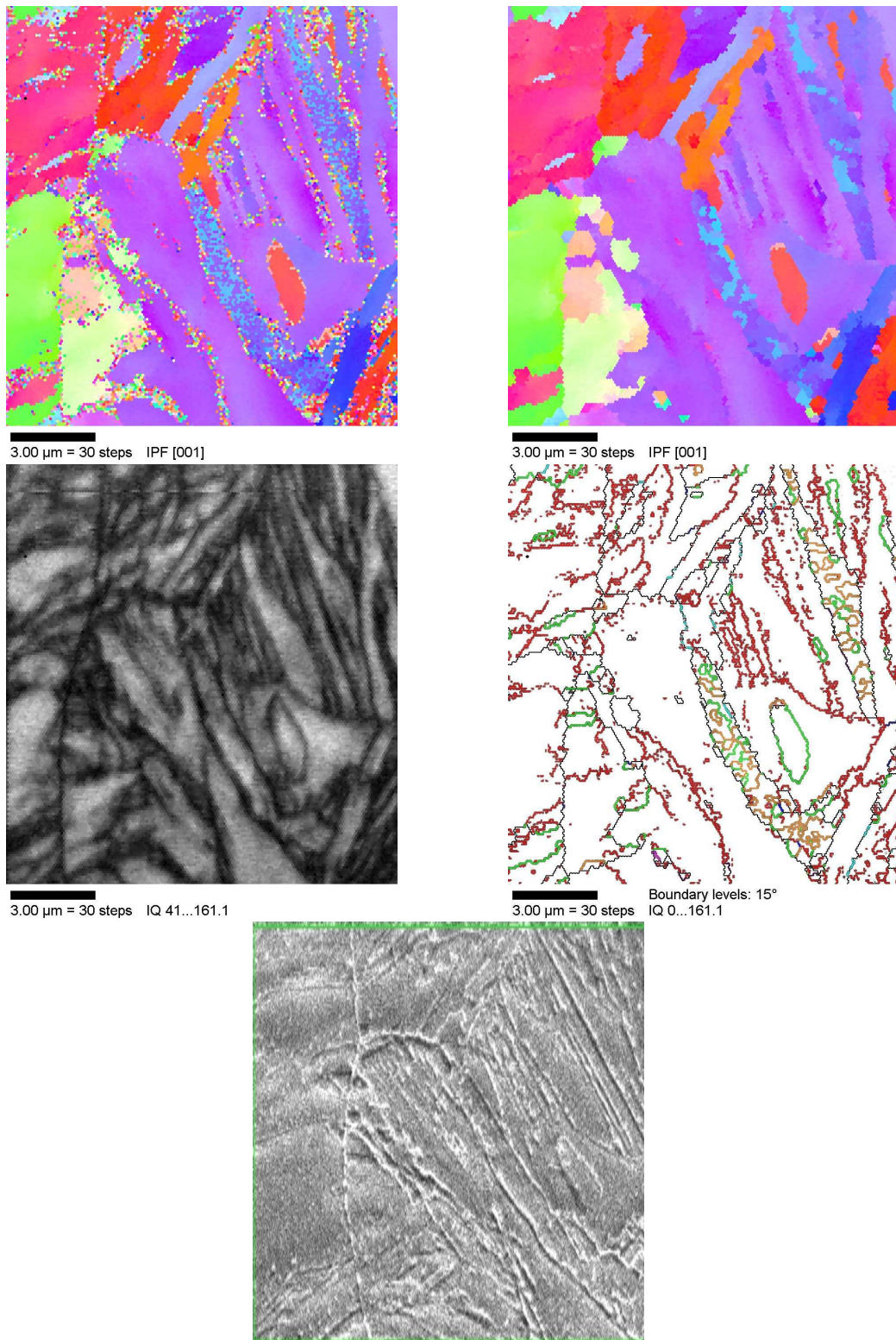


Figure 7.13:  $2\frac{1}{4}$ Cr1Mo steel, 600 °C, 16 hours tempering

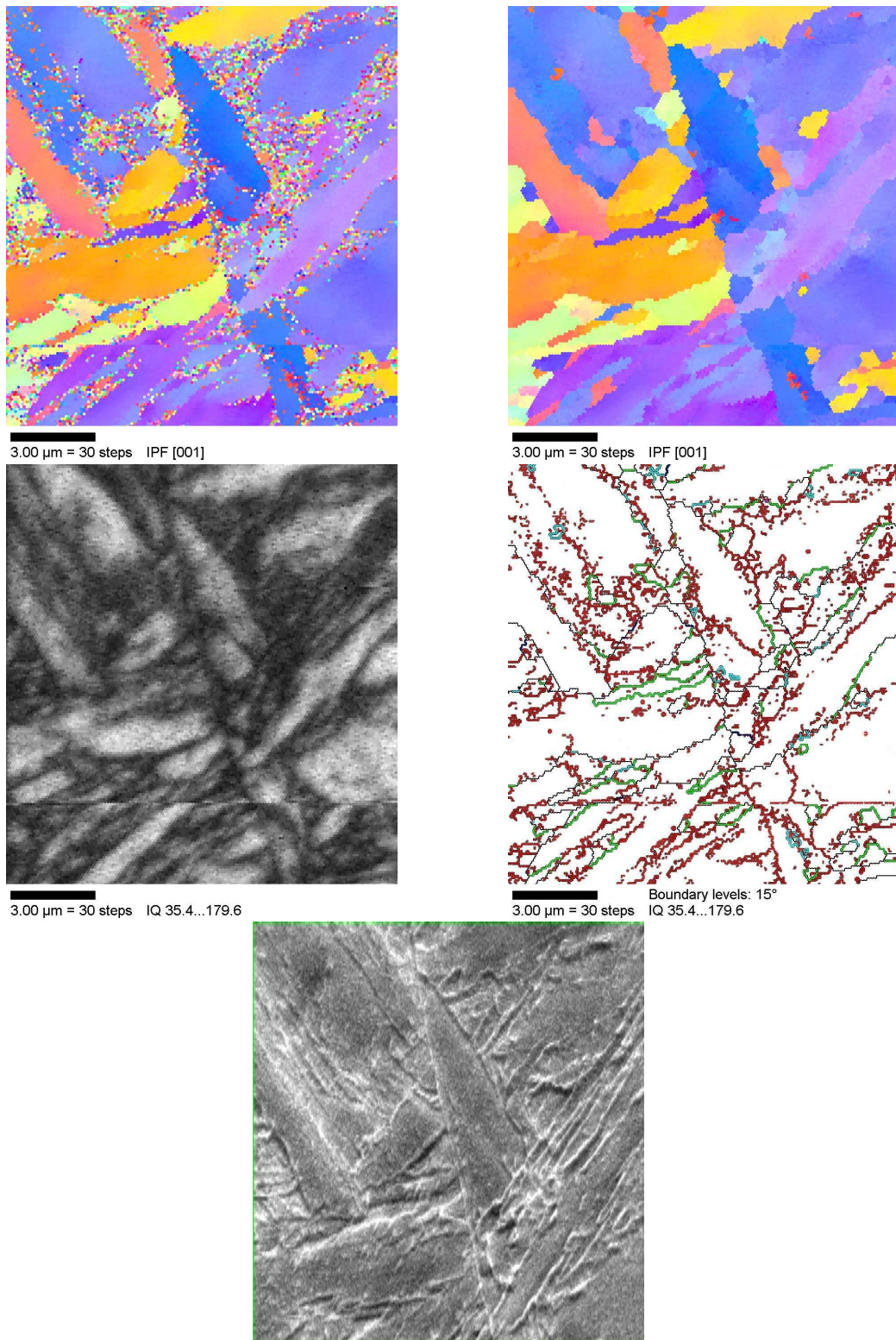


Figure 7.14: 2 $\frac{1}{4}$ Cr1Mo steel, 600 °C, 16 hours tempering

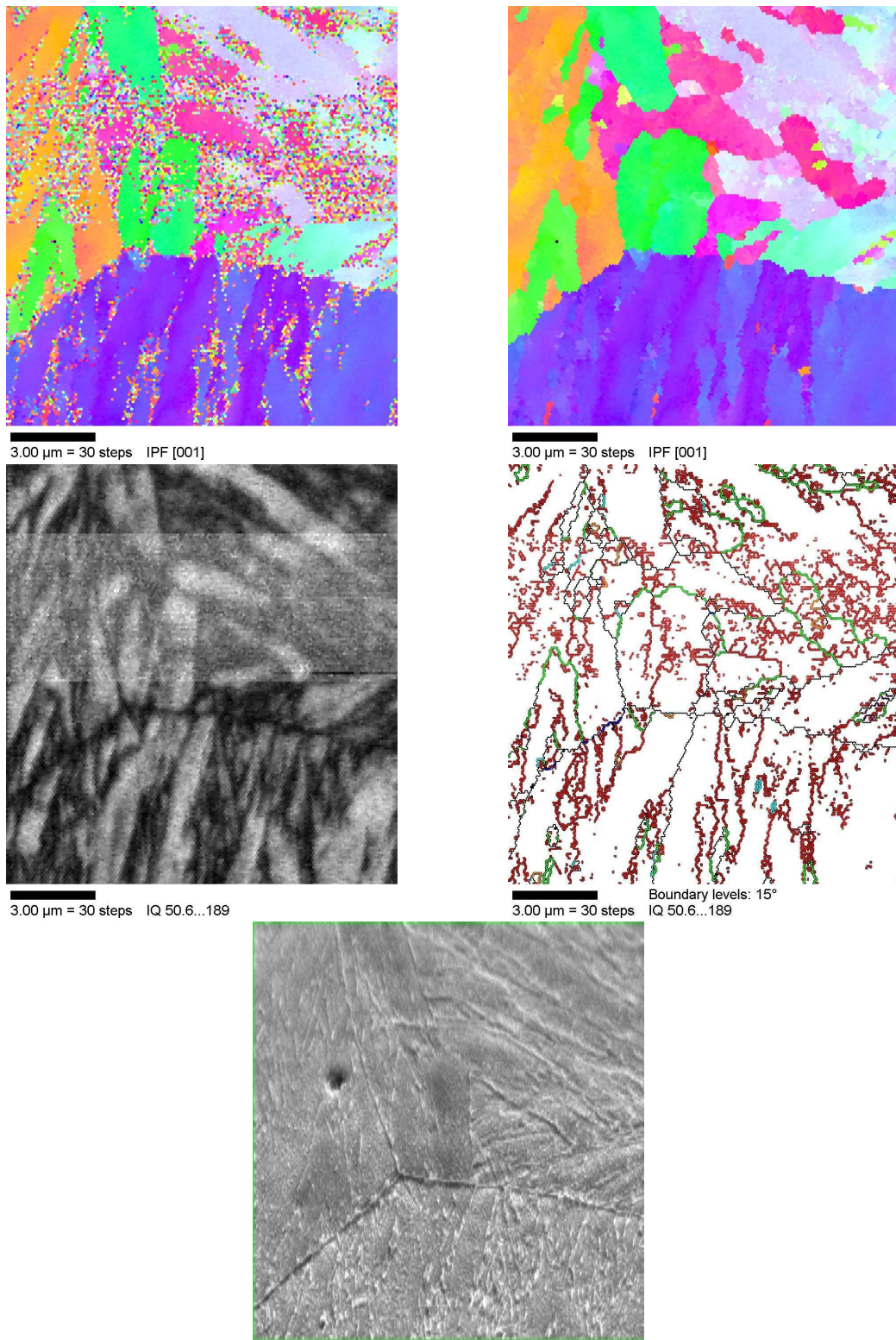


Figure 7.15:  $2\frac{1}{4}$ Cr1Mo steel, 600 °C, 16 hours tempering

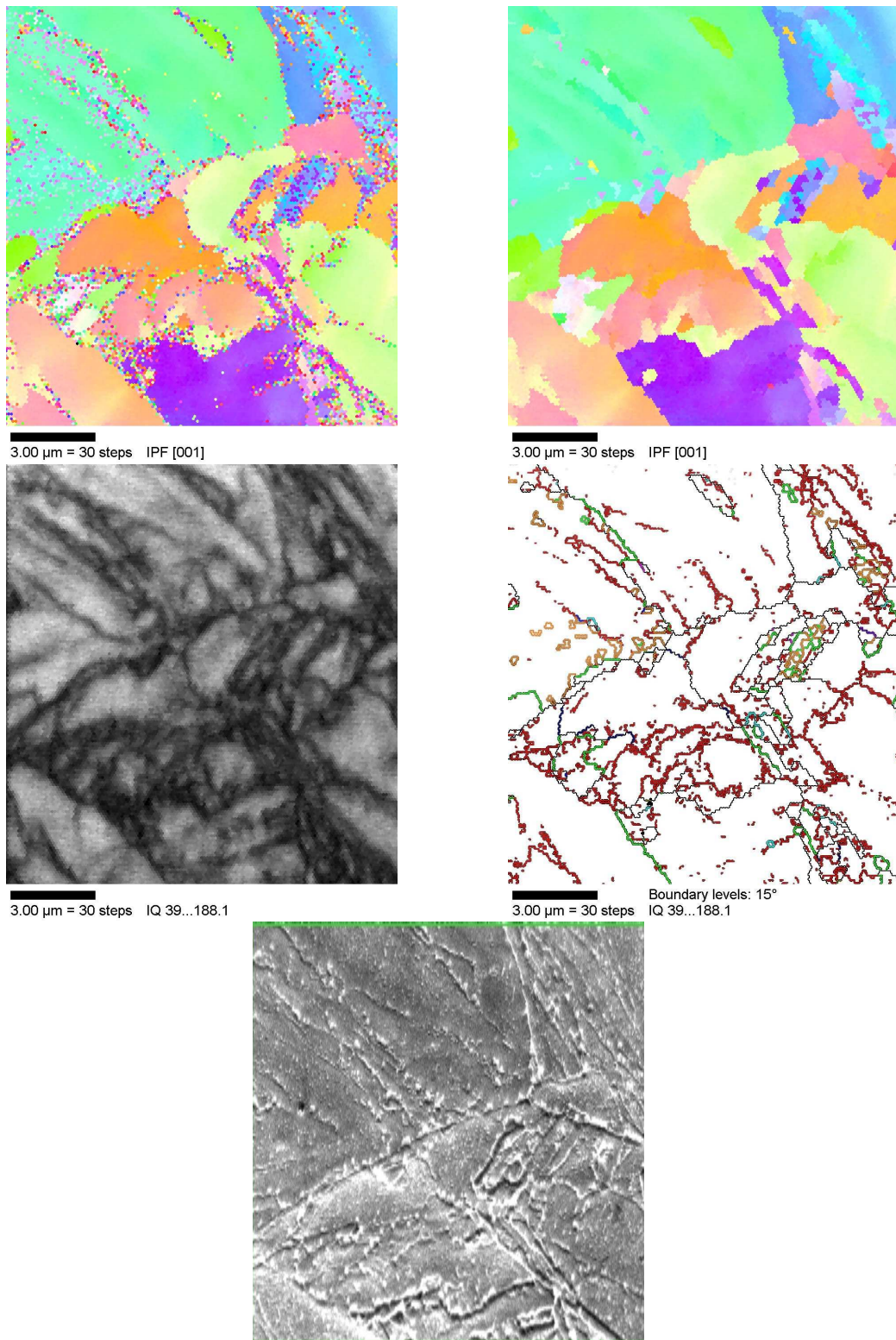


Figure 7.16: 2 $\frac{1}{4}$ Cr1Mo steel, 600 °C, 64 hours tempering

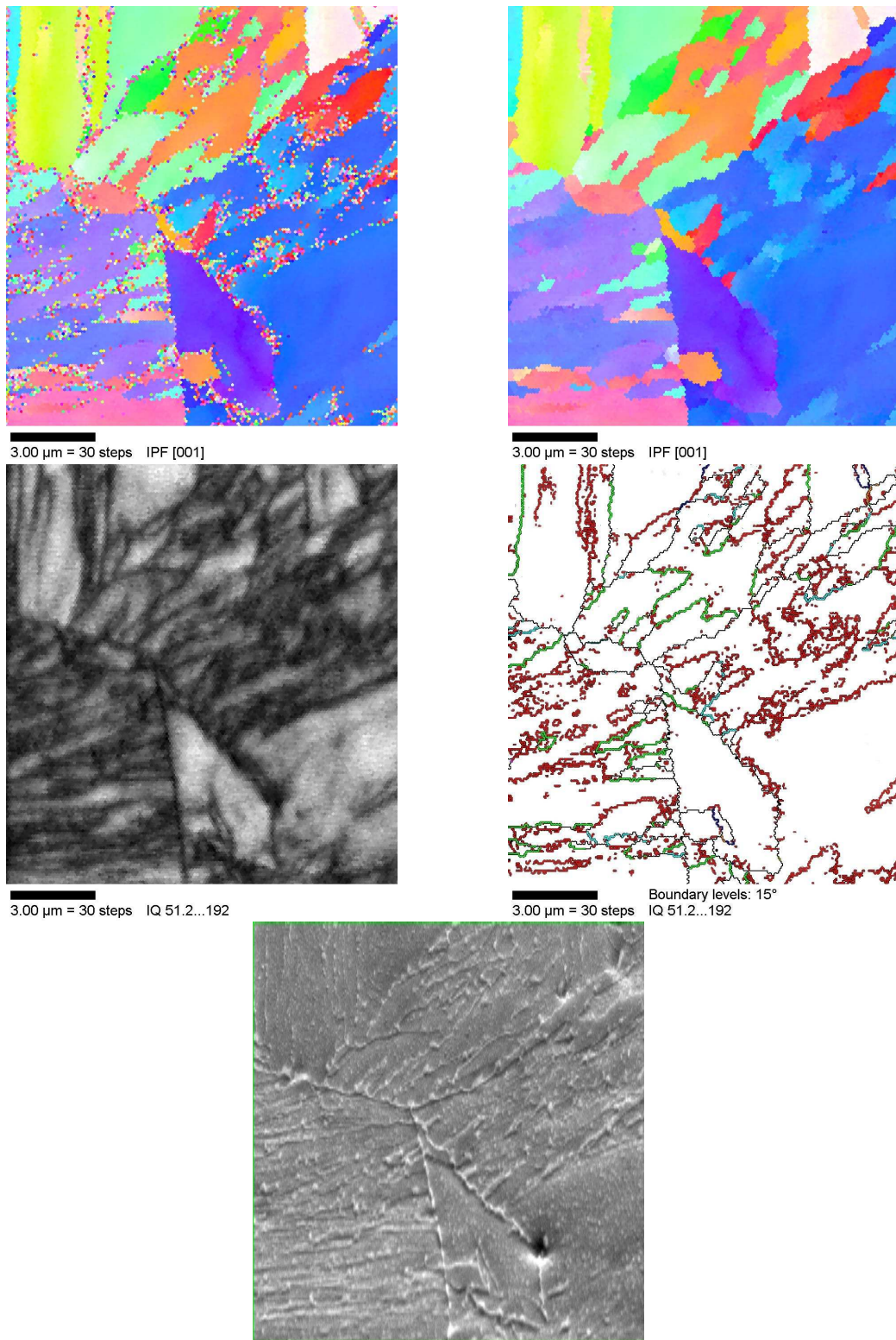


Figure 7.17:  $2\frac{1}{4}\text{Cr1Mo}$  steel,  $600\text{ }^\circ\text{C}$ , 64 hours tempering

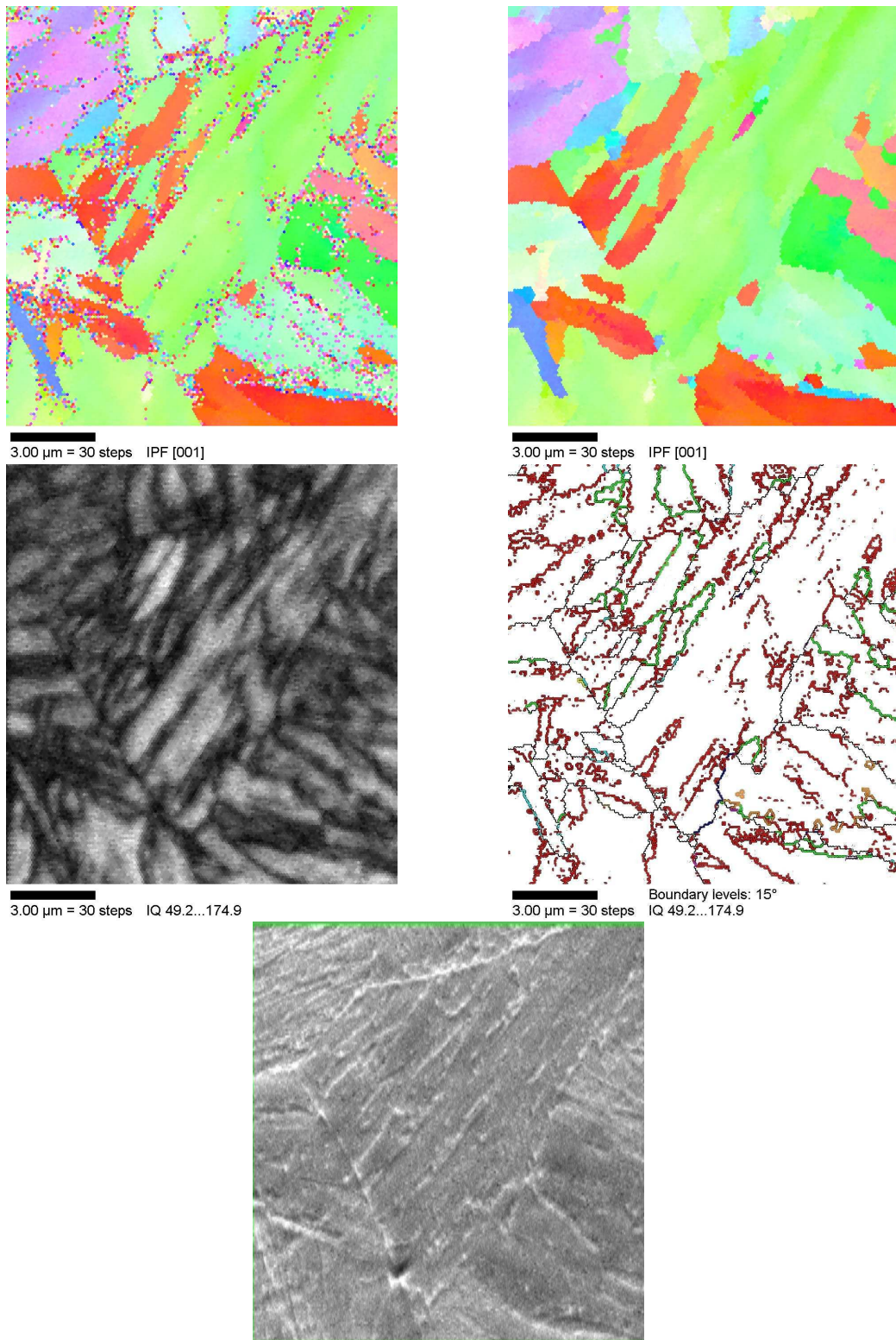


Figure 7.18: 2 $\frac{1}{4}$ Cr1Mo steel, 600 °C, 64 hours tempering

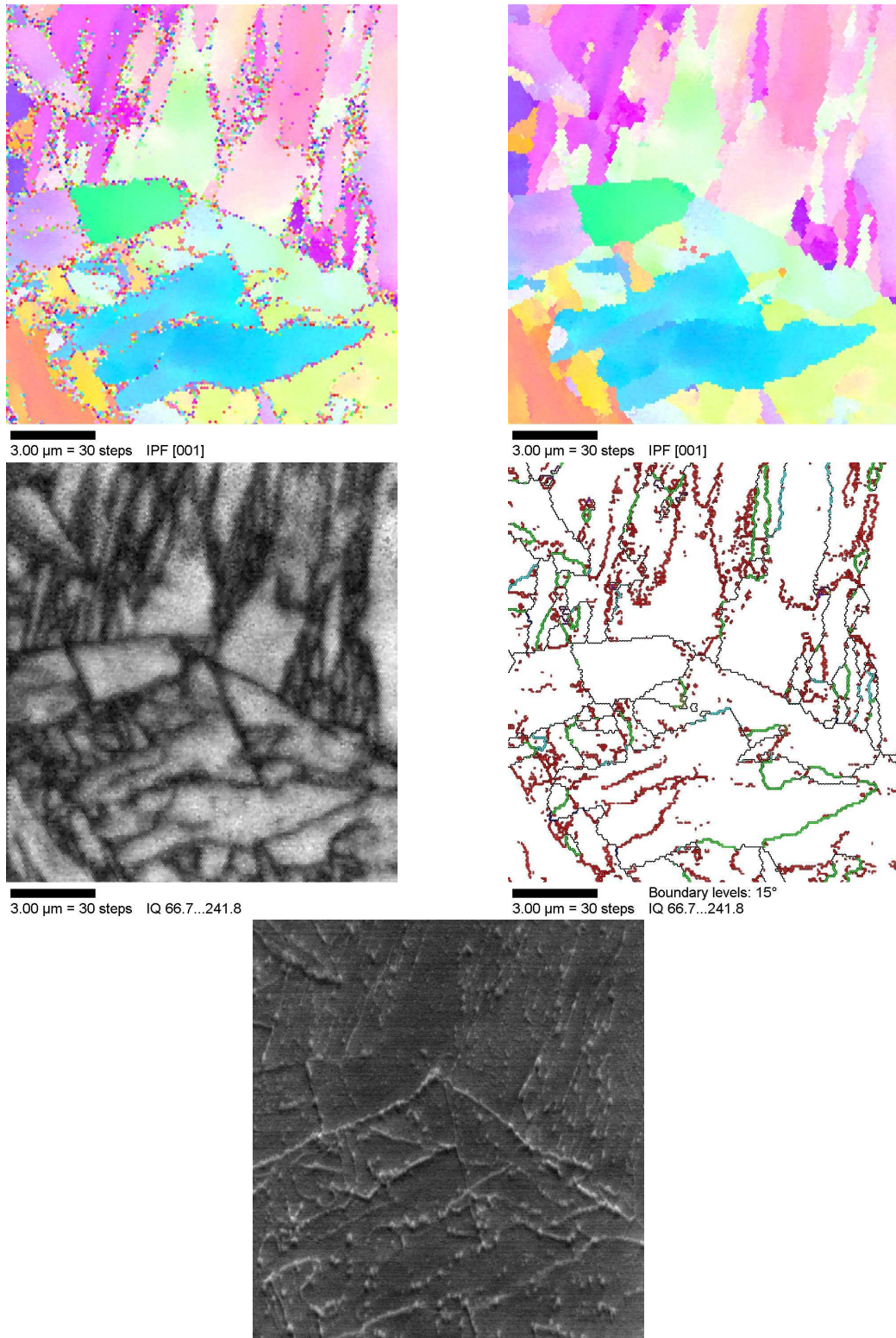


Figure 7.19:  $2\frac{1}{4}$ Cr1Mo steel, 600 °C, 128 hours tempering

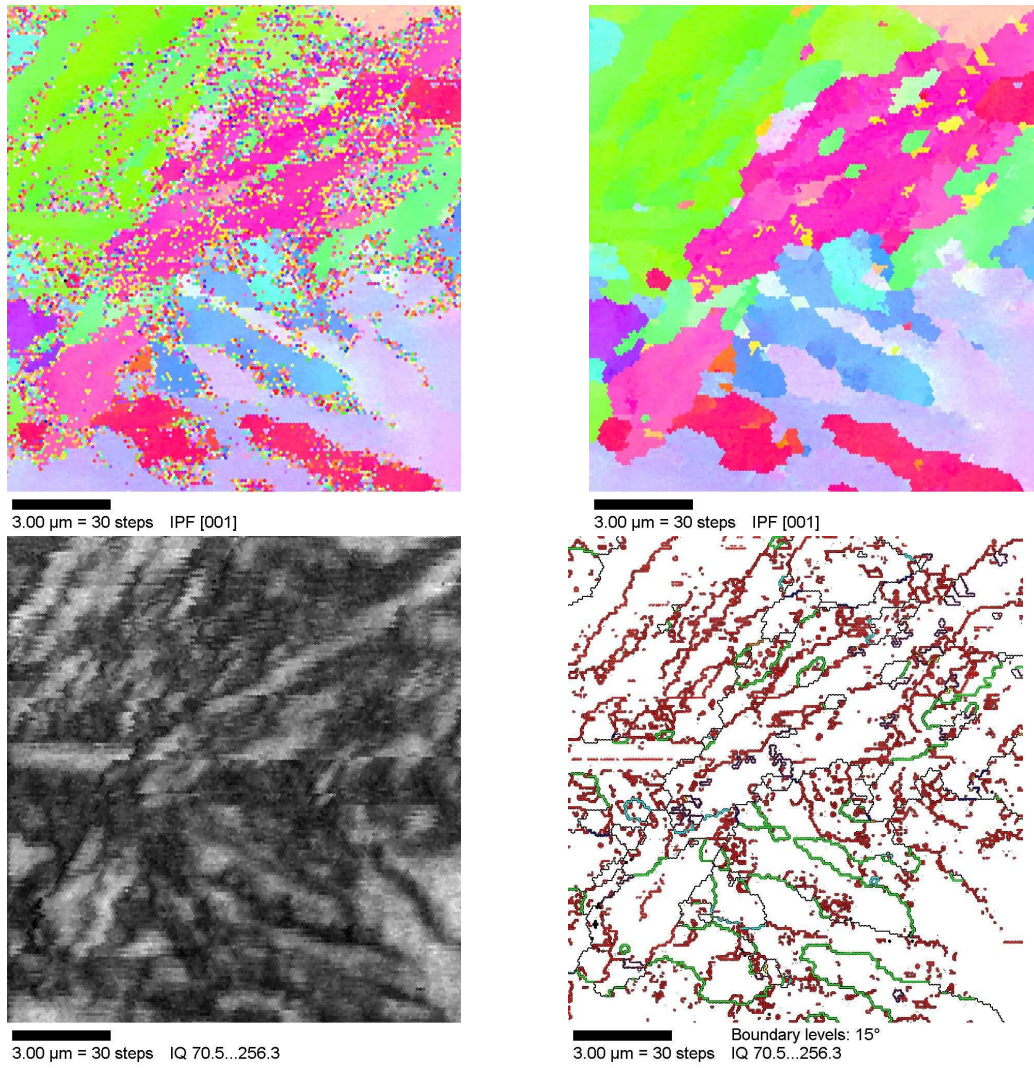


Figure 7.20:  $2\frac{1}{4}$ Cr1Mo steel, 600 °C, 128 hours tempering

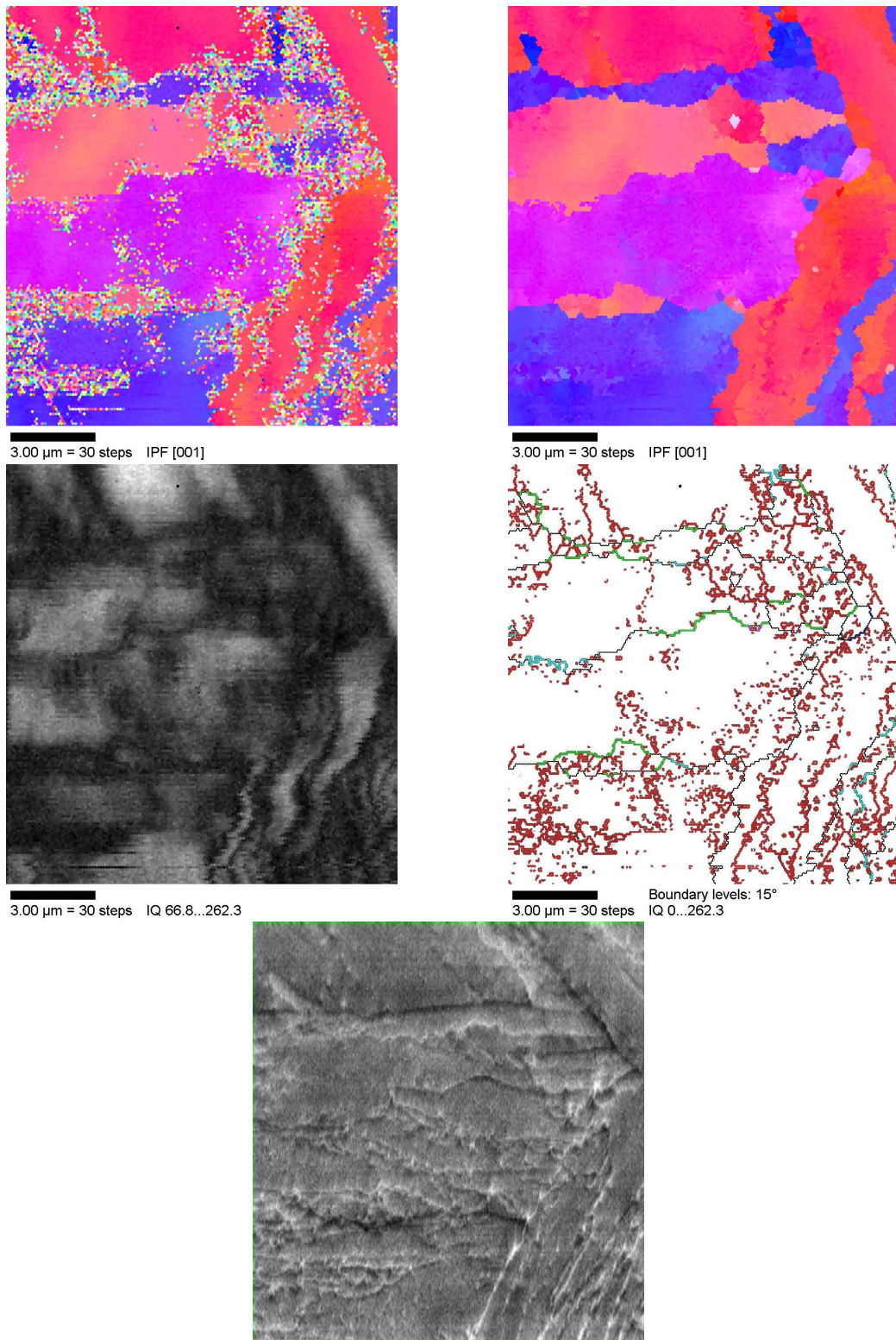


Figure 7.21:  $2\frac{1}{4}$ Cr1Mo steel, 600 °C, 128 hours tempering

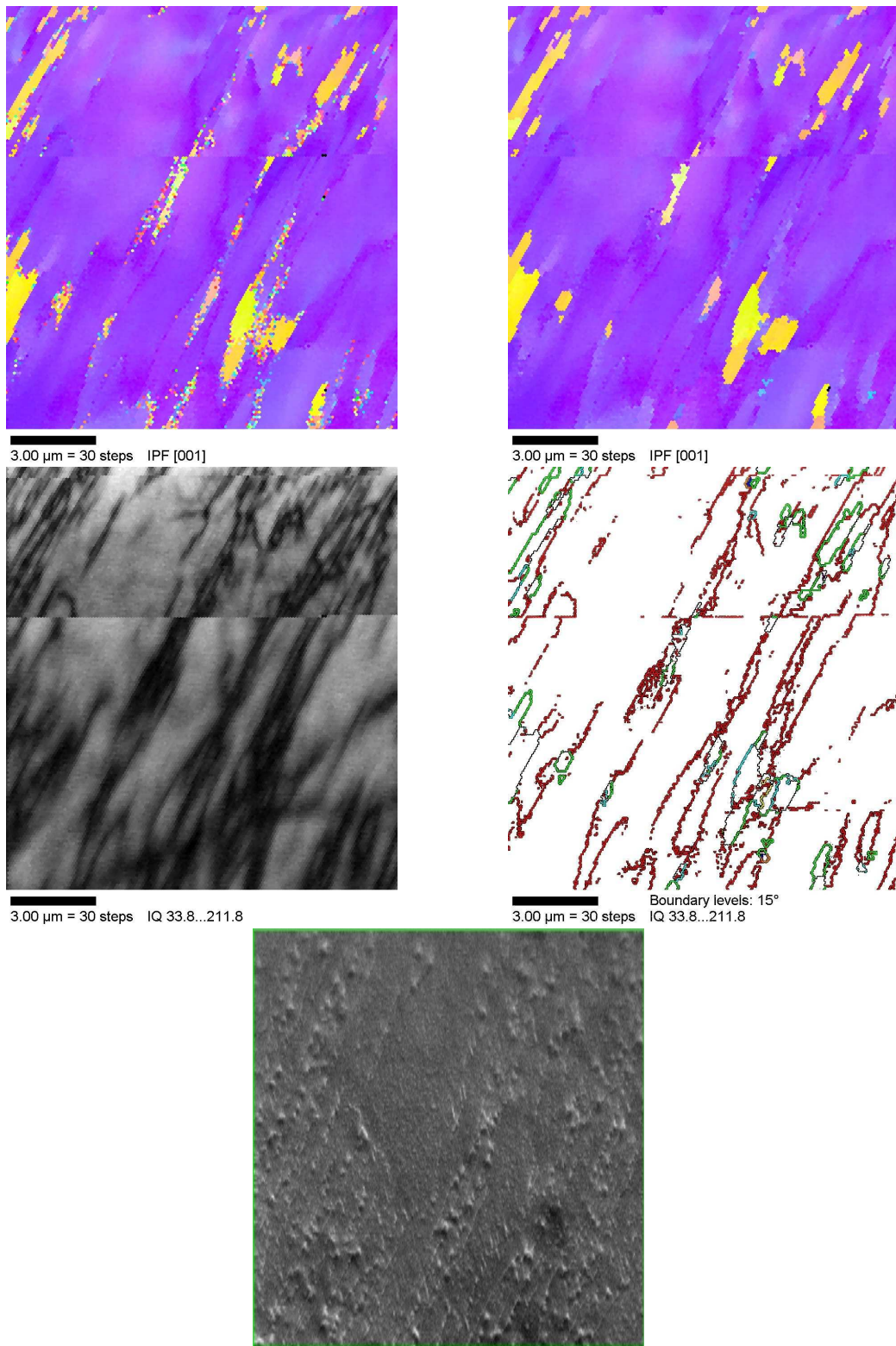


Figure 7.22:  $2\frac{1}{4}$ Cr1Mo steel, 600 °C, 256 hours tempering  
- 187 -

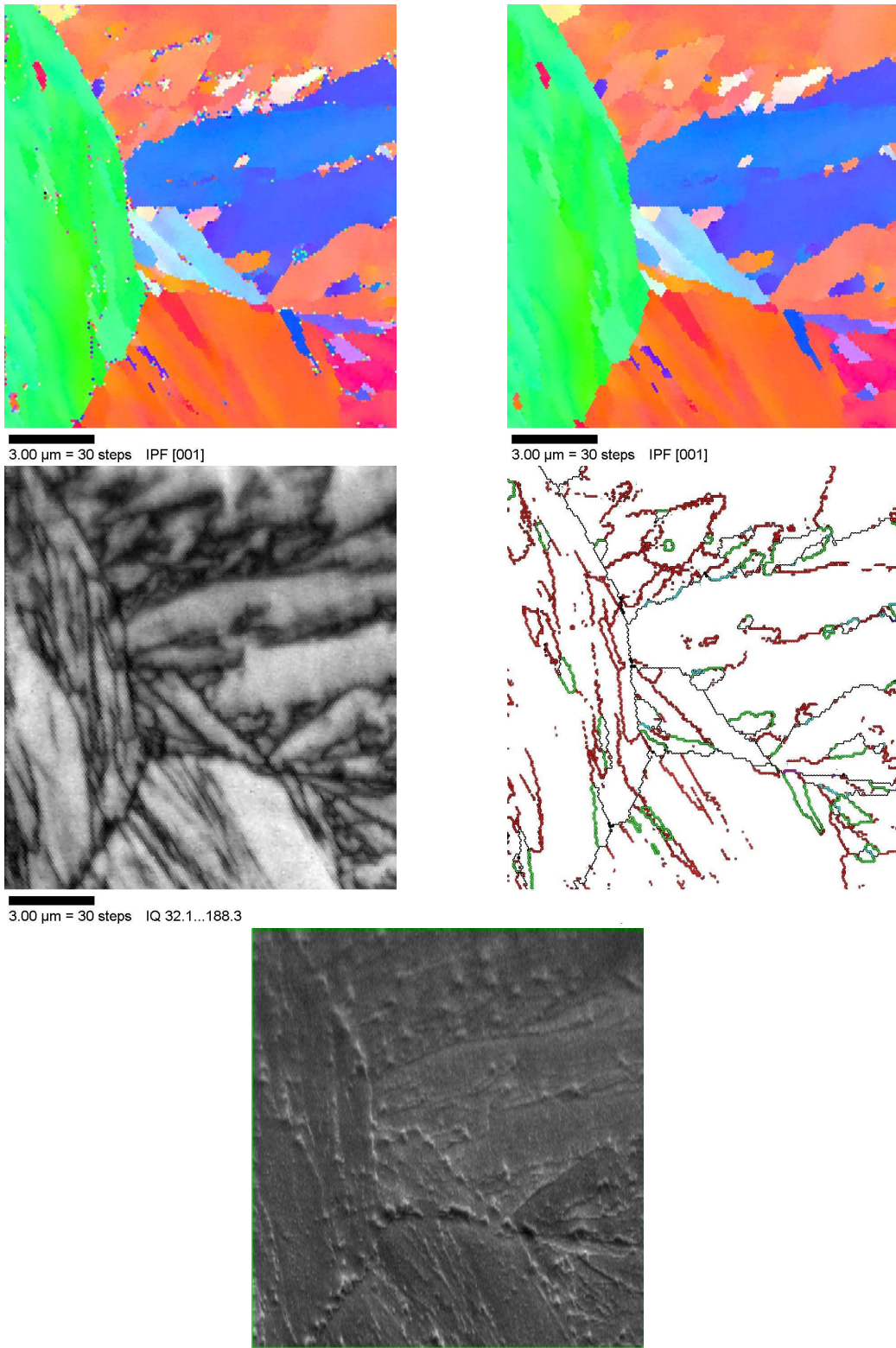


Figure 7.23:  $2\frac{1}{4}$ Cr1Mo steel, 600 °C, 256 hours tempering  
- 188 -

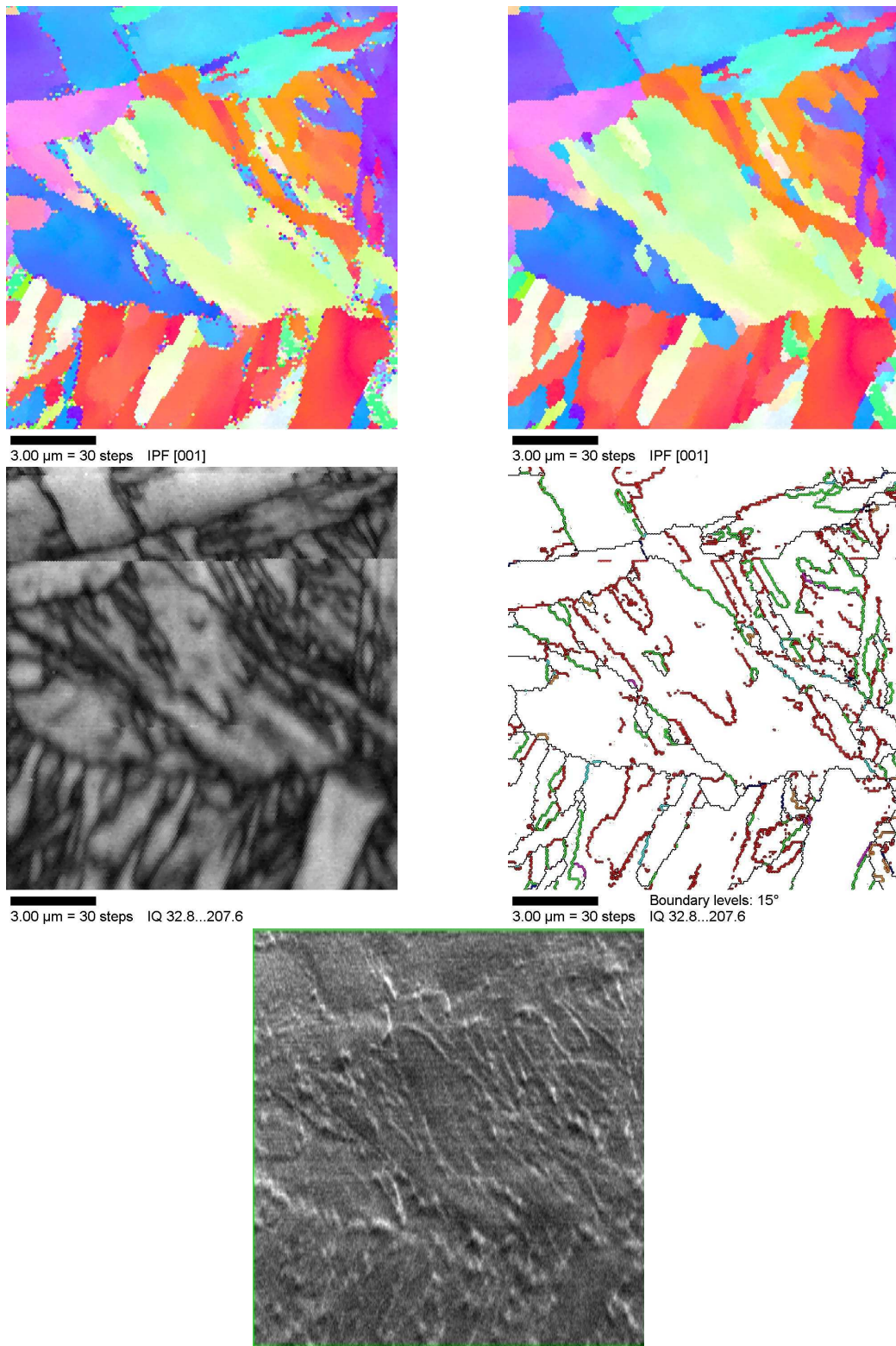


Figure 7.24: 2 $\frac{1}{4}$ Cr1Mo steel, 600 °C, 256 hours tempering

### 7.7.1 As-quenched data

#### Figure 7.7

The raw-data orientation map contains large regions of indeterminate points, which coincide with the areas of lowest image quality. On the cleaned map, there are many small regions which have been constructed by the cleaning algorithm from the available data, but it is not clear which, if any, of these correspond to true grain structures. On Figure 7.25, the regions considered by the software as grains are coloured, and the indeterminate areas are white. The cleaning algorithm was intended to deal with only small numbers of indeterminate points and cannot be expected to make correct estimates over such large areas of uncertainty.

The grain boundary map for this sample may not be reliable because of the large areas of poor IQ. There are many apparent low-angle boundaries which correspond to the small ‘grains’ in the cleaned image and may be spurious. However, the random boundaries on the map correspond reasonably well in shape and position to features on the SEM image.

#### Figure 7.8

An even greater proportion of indeterminate points is present in this image than in Figure 7.7, so the cleaned map and grain boundary map are rather untrustworthy. The extent of the indeterminate areas is visible in Figure 7.25; these correspond well to the dark areas on the IQ map. It is difficult to relate any of the OIM maps to the SEM image.

#### Figure 7.9

Despite being obtained from the same sample as the images in Figure 7.7 and Figure 7.8, this image has little in common with them. The indeterminate point proportion is much lower, and much of the image consists of a single orientation. Long, parallel, vertical features are visible in the central region of the IQ map. Although the SEM image of this region is extremely poor, similar features can just be discerned. Their shape and size suggest that they are individual laths or groups of very few laths, bounded by dis-



3.00  $\mu\text{m}$  = 30 steps Unique Grain Color

As-quenched; Figure 7.7



3.00  $\mu\text{m}$  = 30 steps Unique Grain Color

As-quenched; Figure 7.8



3.00  $\mu\text{m}$  = 30 steps Unique Grain Color

As-quenched; Figure 7.9



3.00  $\mu\text{m}$  = 30 steps Unique Grain Color

600°C, 256 hour tempered; Figure 7.23

Figure 7.25: Maps with regions identified as unique grains marked in colour, and indeterminate regions in white.

located regions. Their misorientation angle is very small; since the grain boundary map shows discontinuous low-angle boundaries in this region, it must be around  $2^\circ$ . In other parts of the image, there are gradual orientation variations without any clearly visible lath boundaries. The red region towards the right-hand side is partly bounded by a  $\Sigma 3$  boundary and may be a twin-related variant of the light-blue orientation.

### 7.7.2 Indeterminate points

The presence of indeterminate points may be due to retained austenite or to martensite tetragonality. The data supplied to the software assumed a body-centred structure, so if other crystal structures were present, their Kikuchi lines would be incorrectly indexed. This would give rise to problems in orientation determination where these phases were prevalent. OIM software can index multiphase microstructures if the correct lattice constants are provided for each, so it is possible to repeat the experiments on these samples to check for other phases. However, another possible origin of the indexing problem is low Kikuchi pattern image quality. This results from high strain and does not depend on the assumed crystal structure. Since regions of low IQ consistently coincide with indeterminate point regions, it is suggested that high strain, rather than incorrect crystal structure data, is the main cause.

### 7.7.3 600°C, 4 hours tempering

#### Figure 7.10

Many indeterminate points are still present after four hours of tempering, but they are more evenly distributed. Laths or groups of laths can be identified by their edges on the image quality map and by small changes at their edges on the orientation map. The grain boundary map contains many, probably spurious, discontinuous boundaries but also some more clearly defined low-angle boundaries with equivalents on the other maps.

**Figure 7.11**

A triple junction of prior austenite grains is visible in the centre of the SEM image. (It appears that the position of the selected region shifted slightly between image and OIM data acquisition so that the junction is not quite central in the OIM maps.) The orientation map contains a combination of wide, homogeneous regions and narrower features with abrupt orientation changes. Some of these may be variants occurring within the same morphological packet. The fraction of indeterminate points is lower than in Figure 7.10, and they are mainly concentrated in boundary regions.

**Figure 7.12**

This image shares many of the features of Figure 7.11, with a mixture of grain and packet sizes. The mottled blue and purple region appears to be a single grain with two, almost equally favourable, solutions to the Kikuchi pattern.

**7.7.4 600°C, 16 hours tempering****Figure 7.13**

After 16 hours, a much more distinct grain structure is visible, with obvious correspondence to the SEM micrograph. The indeterminate points are mainly confined to grain boundaries. A clear random prior austenite boundary runs from top to bottom. The purple region contains many subregions slightly misoriented from one another, and red packets, some of which are bounded by  $\Sigma 3$  boundaries.

**Figure 7.14**

This image has similar features to Figure 7.13, but it appears that the microscope was shaken toward the end of image acquisition since there is a jolt in the micrograph. This can be caused by mechanical vibrations or spontaneous beam jumping (Kawahara, personal communication). The effect is not easily visible in the orientation maps but produces a spurious ‘low-angle boundary’ in the boundary map.

**Figure 7.15**

The purple area at the bottom of the image is composed almost entirely of slightly misoriented subregions, whose boundaries correspond to low-IQ features. The bright-coloured band on the IQ map is an artefact of the measuring process. In this type of FEG-SEM, the beam intensity tends to decrease with time, especially just after starting up the microscope. This sometimes requires adjustments of the settings during data acquisition so that the beam intensity is sufficient to obtain backscatter data. This adjustment changes the image quality, giving a bright band (Kawahara, personal communication).

**7.7.5 600°C, 64 hours tempering****Figure 7.16 and Figure 7.17**

These images have inhomogeneous distributions of image quality and grain or packet sizes. The grain boundary maps correspond well to the SEM and IQ images, particularly in Figure 7.17, which is also notable for a large number of  $\Sigma 3$  boundaries. By comparison with the SEM image, it appears that some of these are boundaries between variants within the same morphological packet.

**Figure 7.18**

The green and orange areas separated by  $\Sigma 3$  boundaries in the centre of this image also appear to be variants within a morphological packet. Parallel-sided, slightly misoriented features are present within the green area; these appear to be groups of laths similar to those in the centre of Figure 7.9, but with a reduced dislocation density.

**7.7.6 600°C, 128 hours tempering****Figure 7.19**

Particularly noticeable in this image are grains or packets with gradual changes of orientation. Over a single grain, the colour can change from green

to white over a distance of 3  $\mu\text{m}$  without any low-angle boundaries. In the IQ map, these grains are of lighter colour and appear relatively strain-free.

### Figure 7.20 and Figure 7.21

From the IQ maps of both of these images, it is clear that serious shaking has occurred. Some impression of the orientations and grain structures can be inferred from these maps, but they are not suitable for detailed study.

### 7.7.7 600°C, 256 hours tempering

#### Figure 7.22

This interesting region consists of one orientation, in purple, with small yellow ‘islands’ of a different orientation embedded within it. Many of the islands are bounded by  $\Sigma 3$  (green) or  $\Sigma 11$  (turquoise) boundaries. The image forms part of a single morphological packet, as shown by the parallel lines on the SEM image, but appears different from the ‘block’ model discussed by Gourgues *et al.* (2000).

A spurious ‘low-angle boundary’ arising from beam jumping, is present about a third of the way down the image.

#### Figure 7.23

This raw image contains especially few indeterminate points, and changes very little on cleaning. The IQ map has many light-coloured regions, and the dark regions are narrow and coincide with grain boundaries. The prior austenite grains meeting in the centre contain slightly misoriented regions and small, included regions with  $\Sigma 3$  boundaries in a similar way to the region in Figure 7.22. The orange and blue regions near the top appear, from the SEM image, to be blocks within the same packet.

The small light blue triangle in the centre is bounded on all sides by random boundaries, with no clear relationship to any of the surrounding regions, but its striped structure suggests that it is a prior austenite grain with a former martensite lath substructure, rather than a recrystallisation nucleus.

**Figure 7.24**

The grains and packets in this image are on a smaller scale than those of Figure 7.22 and Figure 7.23. Clear, parallel-sided former groups of laths are evident, as are  $\Sigma 3$  and  $\Sigma 11$  boundaries.

**7.7.8 Summary**

The as-quenched data can have very low image quality and a large number of indeterminate points. This is thought to arise from the high levels of strain present after quenching. Tempering improves the IQ and increases the number of points whose Kikuchi patterns can be solved. It is therefore not entirely clear whether tempering changes the orientations significantly or simply helps to reveal the existing microstructure by relaxing the strain.

A typical crystallographic packet in the tempered structure contains many slightly misoriented subunits arising from groups of martensitic laths. Small regions of crystallographically related variants may be embedded in the main variant. These often have  $\Sigma 3$  or  $\Sigma 11$  boundaries. Wide variations in crystallographic packet sizes are possible, from less than a micron to the majority of the micrograph area.

No evidence of recrystallised structure can be seen; instead, even after 256 hours of tempering, the martensitic lath orientation relationships are preserved.

**7.8 Statistical analysis****7.8.1 Grain boundary misorientations**

The misorientation angles between adjacent points were calculated, and their distribution plotted, for both raw and cleaned data. Figure 7.26, Figure 7.27 and Figure 7.28 demonstrate that there is a wide variation of misorientations in the raw data. The cleaned data for the AQ sample have a variety of peaks, at low angles,  $30^\circ$ ,  $45^\circ$  and  $50\text{--}60^\circ$ . After intermediate tempering, there is more consistency between data sets, and well-defined peaks are present at low angles,  $30^\circ$  and  $50\text{--}60^\circ$  (Figure 7.27). Prolonged tempering suppresses

the  $30^\circ$  peak (Figure 7.28). In the raw data, the indeterminate points contribute to the statistics of misorientations, and it is only by removing them that real relationships can be revealed. However, as discussed above, the cleaning algorithm is not infallible, especially when there are many indeterminate points, so the data from longer tempering times are probably more trustworthy than those from the AQ and 4 hour samples.

These observations agree well with those of Gourgues *et al.*, who also detected a peak at  $60^\circ$ .

### 7.8.2 Coincidence boundaries

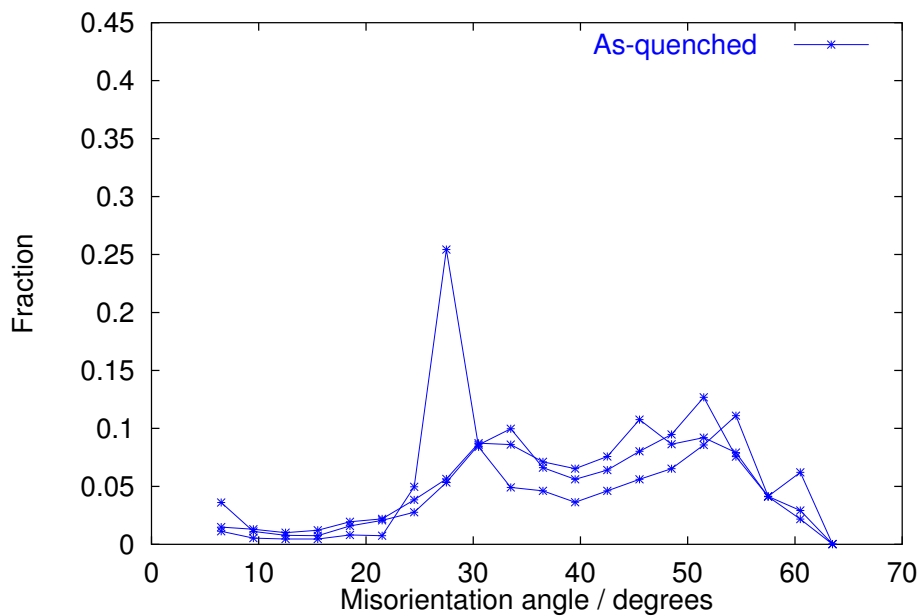
Figure 7.29 shows the variation in the fraction of low-angle,  $\Sigma 3$  and random boundaries, as obtained from the cleaned data, with tempering time. In all of these specimens, the fraction of boundaries of any other type than these three is extremely small. Only one set of data was included for 128 hours because of the image shaking problem affecting the other sets. A decrease in the low-angle boundary fraction and an increase in  $\Sigma 3$  and random boundaries occurs during tempering. This may be a real phenomenon, or simply the result of the disappearance of spurious low-angle boundaries arising from indeterminate points and cleaning.

Low-angle and random boundaries are the predominant types, with a significant minority of  $\Sigma 3$ . It can be seen by inspection of grain boundary maps that prior austenite boundaries are always random, and the internal structure of prior austenite grains contains many low-angle boundaries, some  $\Sigma 3$  and some random boundaries.

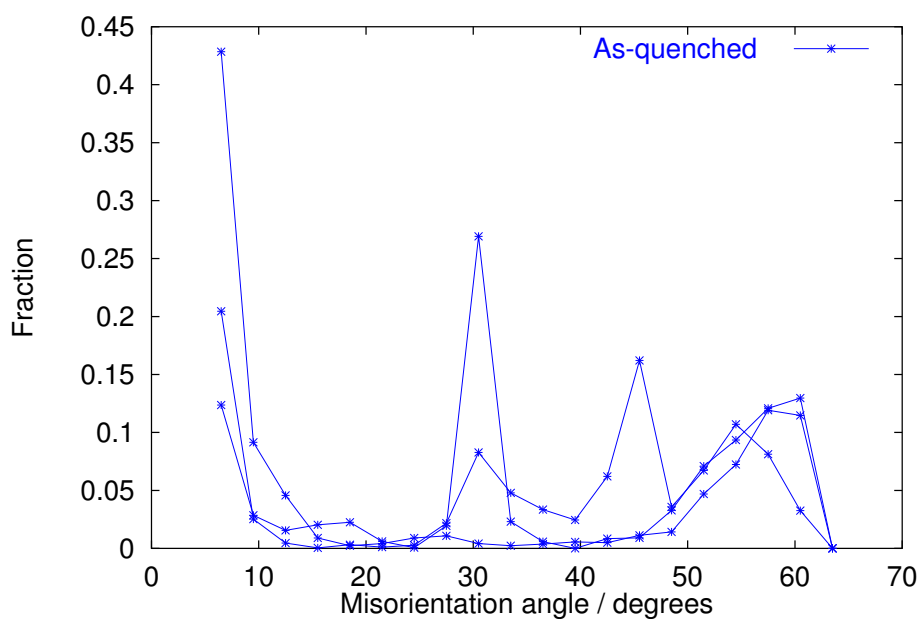
### 7.8.3 Statistics of indeterminate points

The number of indeterminate points in each image was quantified by generating an image similar to those in Figure 7.25 and converting it to a black-and-white image as shown in Figure 7.30. An image analysis program, 'ImageTool', was then used to determine the fraction of the image occupied by black points.

Figure 7.31 shows the relationship between the indeterminate point frac-



Raw data



Cleaned data

Figure 7.26: Misorientation angle distributions for AQ data.

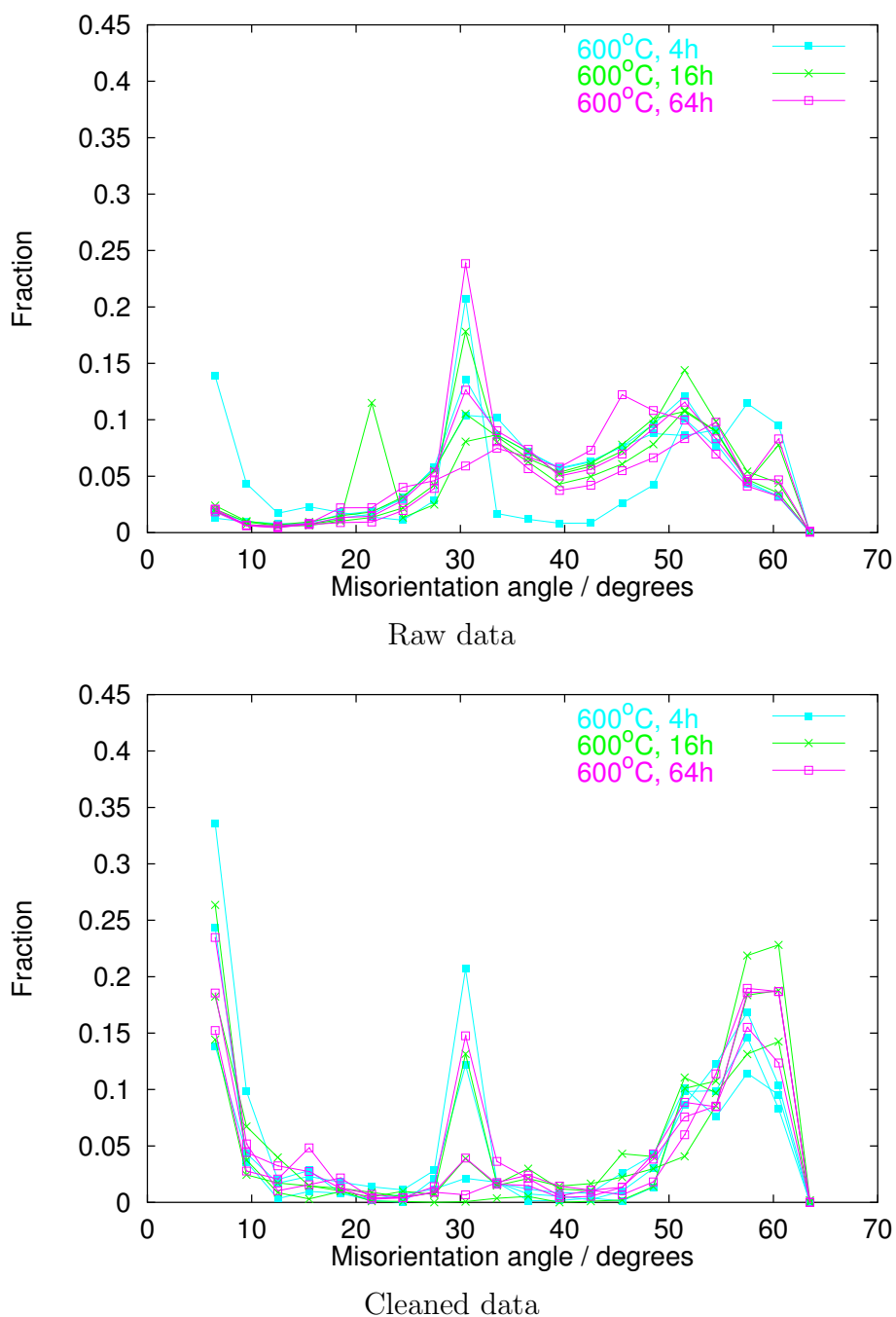


Figure 7.27: Misorientation angle distributions for intermediate tempering times (4–64 hours).

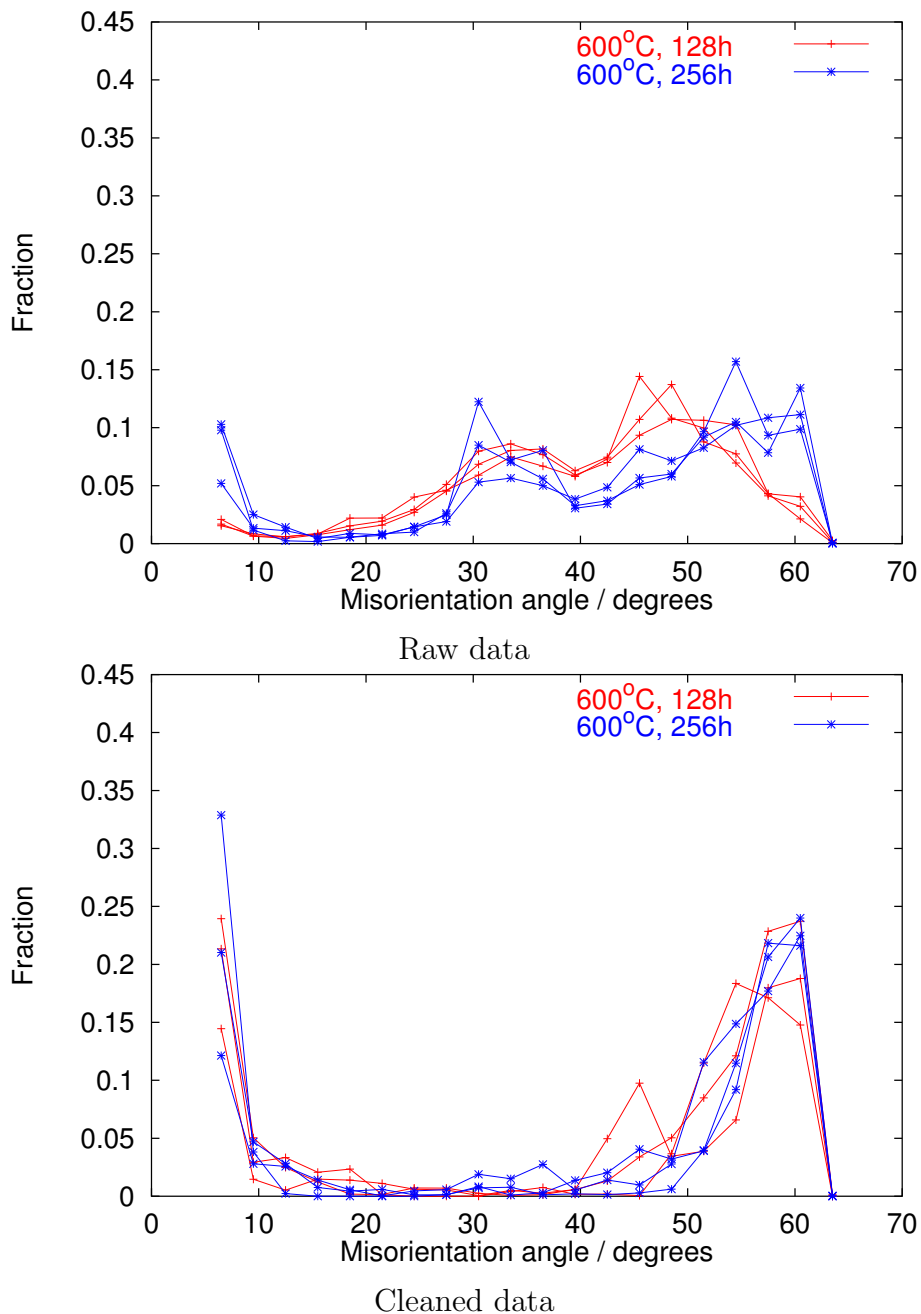


Figure 7.28: Misorientation angle distributions for prolonged tempering (128–256 hours).

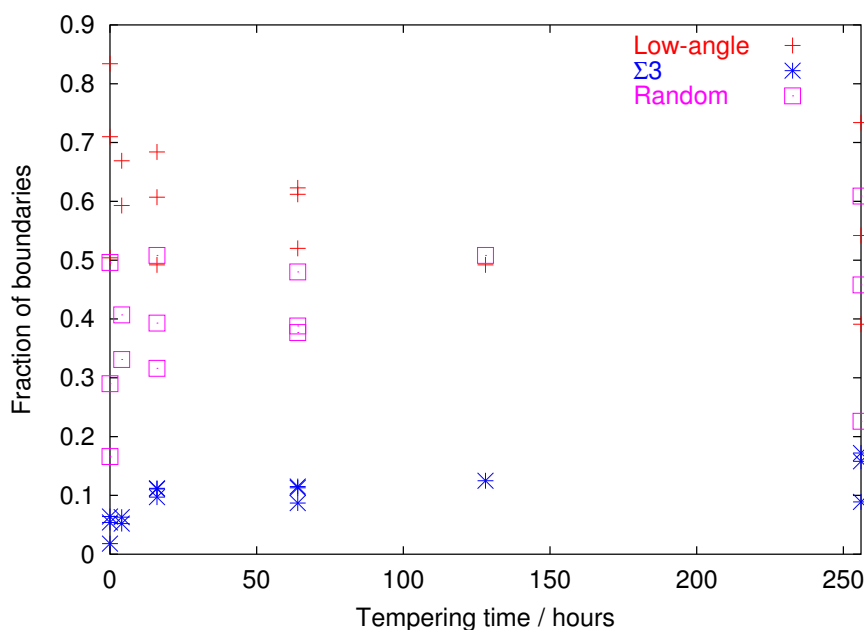


Figure 7.29: Variation in the fraction of low-angle,  $\Sigma 3$  and random boundaries.

tion and tempering time. The two 128 hour images subject to shaking were again excluded. Large variations are seen in this fraction in the AQ and 4 hour samples, but at longer tempering times, a steady decrease is seen.

#### 7.8.4 Image quality statistics

‘ImageTool’ was used to count the pixels of each grey level present in the IQ micrographs. Black is represented by zero, and white by 256. In the AQ samples, wide variations in grey level distributions are seen; dark levels predominate in two of the samples, but in the other, the levels are more evenly spread (Figure 7.32). A higher proportion of lighter greys is seen for intermediate tempering, and after prolonged tempering, there is a noticeable reduction in the proportion of dark levels (Figure 7.33). Grey level data are not fully quantitative, and variations can occur during data acquisition (Figure 7.15), but an indication of the strain reduction can be seen. The grey level data sets from different points on the 256 hour sample are very similar,

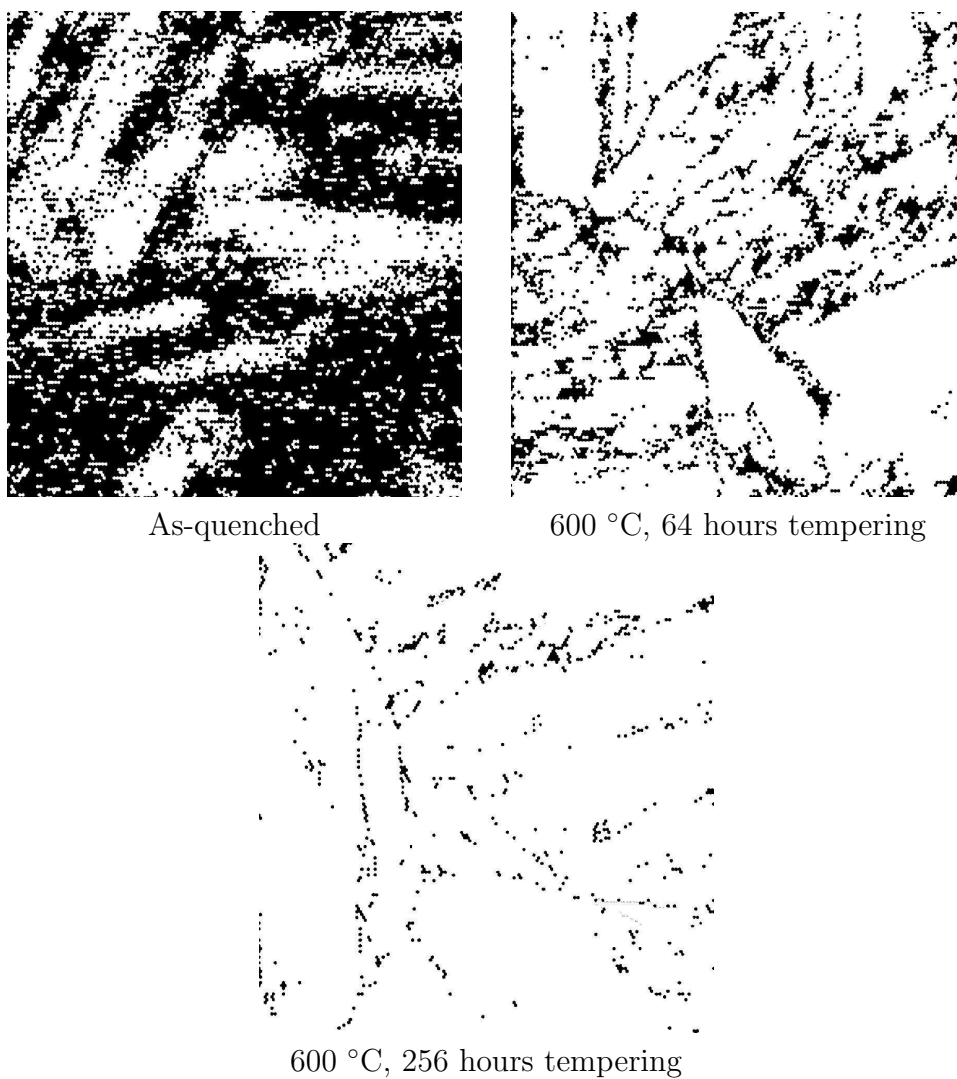


Figure 7.30: Evolution of the number of indeterminate points (in black) with tempering time.

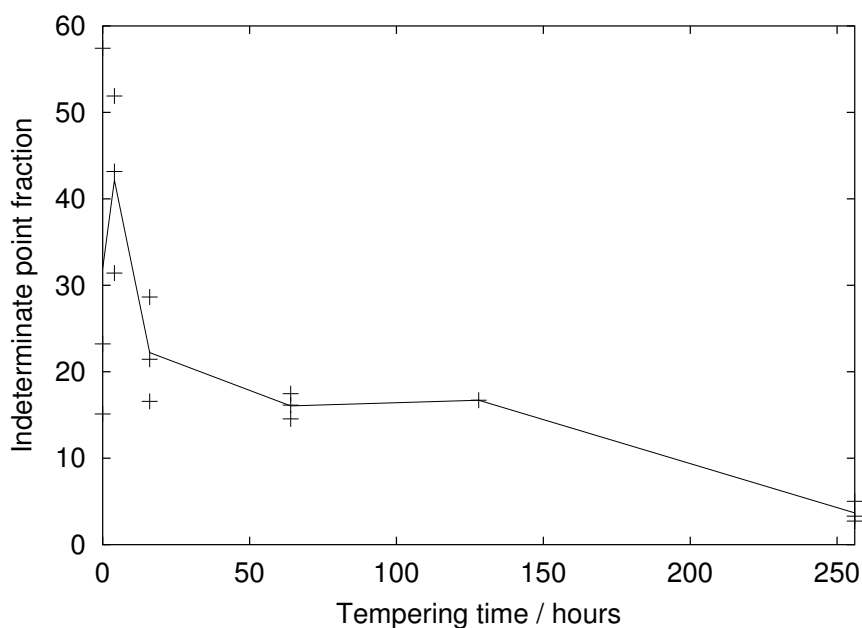


Figure 7.31: Variation in the fraction of indeterminate points.

so it appears that the strain level not only decreases but also becomes more homogeneous after prolonged tempering.

## 7.9 Orientation relationships

Two of the images, Figure 7.9 and Figure 7.22, come from regions within single prior austenite grains. The data sets for these images were selected for closer analysis. In addition to the individual point-by-point data, the software can calculate average orientation values for each region which it identifies as a grain. These data were used to study orientation relationships. (The alternative method, using adjacent points at grain boundaries to calculate misorientations, is subject to the problem of indeterminate points, as was seen above.)

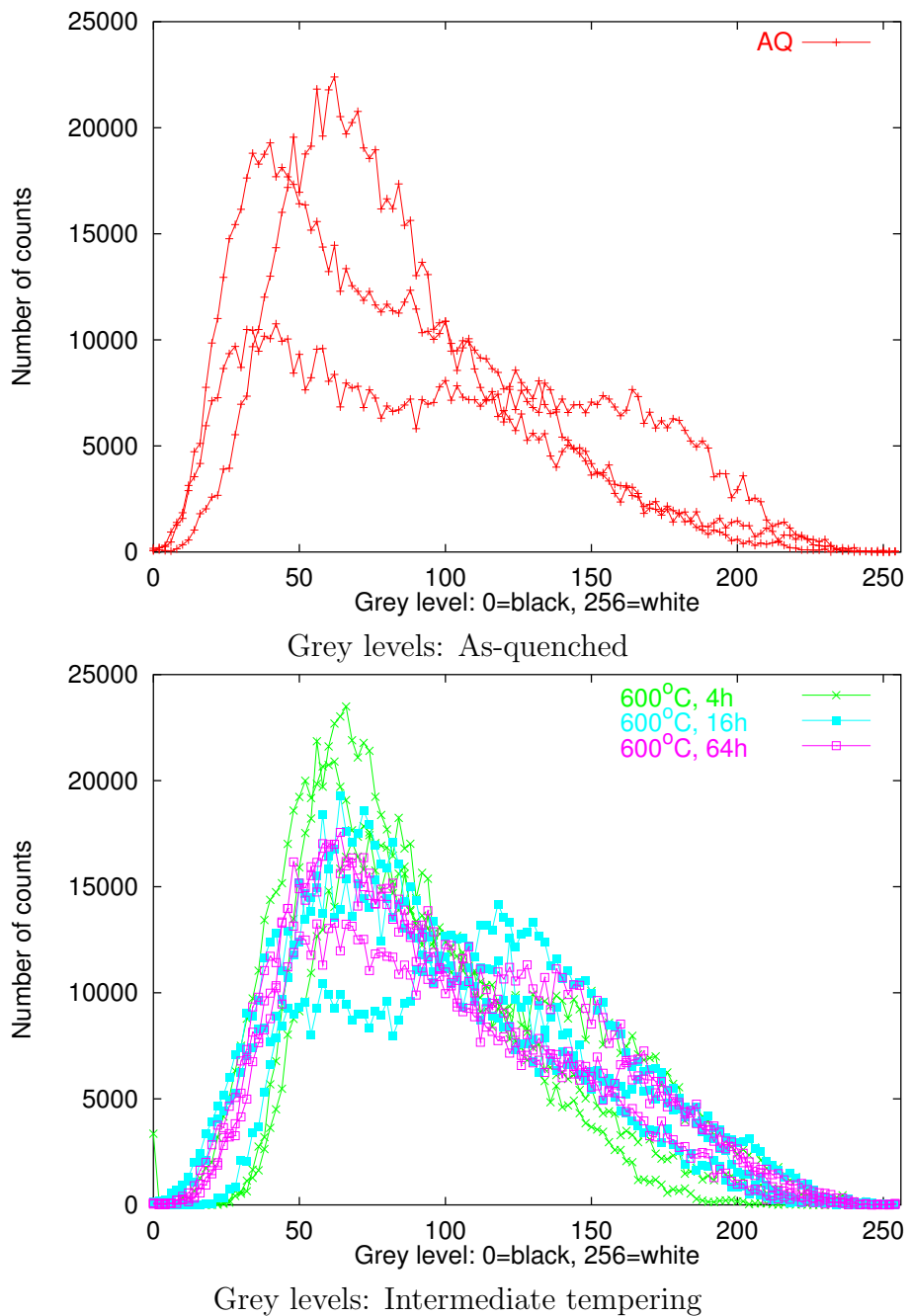


Figure 7.32: Grey levels in AQ and intermediate tempering samples.

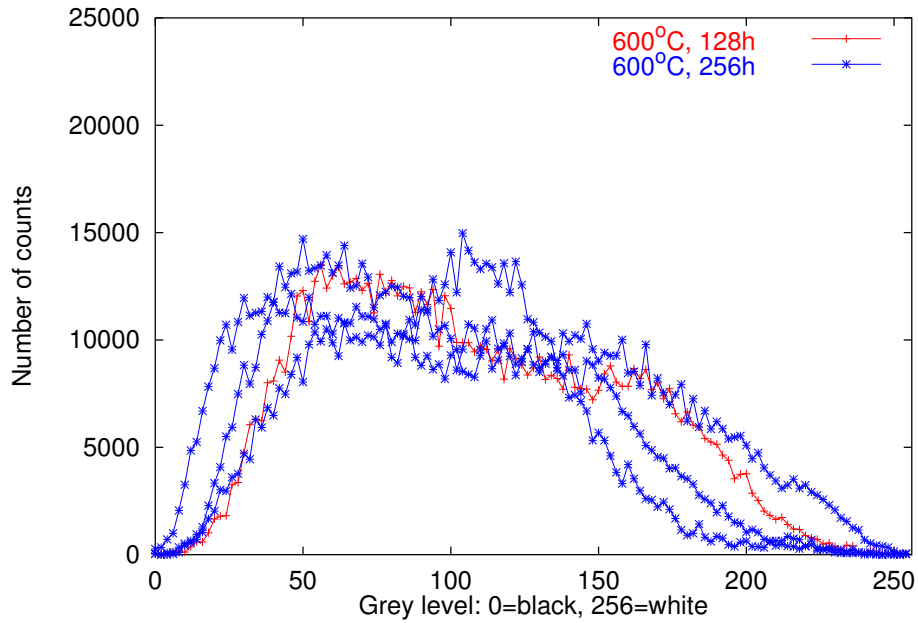


Figure 7.33: Grey levels for prolonged tempering.

### 7.9.1 256 hour sample

The Euler angles of the grains in the 256 hour sample, Figure 7.22, could easily be separated into six groups of similar values. Only one of the 160 distinct grains identified fell outside any of these groups. Table 7.1 lists the number-average Euler angles and the total area occupied by each of the groups. Orientation I occupies by far the greatest area; this is the large purple area in Figure 7.22. The areas of orientations II and III are also significant, but those of the remaining three groups are very small.

The closest  $\Sigma$  values for the interrelationships between these orientations were calculated using a program written by Dr K. Kawahara, Tohoku University. These are listed in Table 7.2 together with Brandon's ratio to quantify the deviation from exact coincidence. Orientation I has a near- $\Sigma 3$  relationship with four of the other orientations. II and III had an angle-axis pair of  $46^\circ \langle 0.03, -0.86, -0.49 \rangle$  rather than  $60^\circ \langle 111 \rangle$ . Some relationships close to  $46^\circ \langle 0.03, -0.86, -0.49 \rangle$  were also found between other pairs of orientation components. (These are not shown in Table 7.2.)

No.	$\phi_1$	$\Phi$	$\phi_2$	Area / $\mu\text{m}^2$
I	334.5	37.3	49.9	187.4
II	230.3	23.3	101.2	7.4
III	100.8	20.6	250.9	4.6
IV	158.5	36.4	218.6	1.0
V	47.2	38.2	301.7	0.3
VI	279.5	38.2	62.5	0.02

Table 7.1: Orientation components found in 256 hour tempered sample.

Pair		Relationship	Brandon's ratio
I	II	$\Sigma 3$	0.93
I	III	$\Sigma 3$	0.80
II	III	$\Sigma 15$	0.97
I	IV	$\Sigma 3$	0.70
I	V	$\Sigma 3$	0.82
I	VI	Random	2.00 from $\Sigma 3$

Table 7.2: Relationships between different orientations in 256 hour tempered sample.

### 7.9.2 AQ sample

The AQ data in Figure 7.9 contained four main Euler angle sets (Table 7.3). The relationships between these show that I and II are very similar in orientation, as are III and IV (Table 7.4). It is clear from the area fractions that I and II constitute the large turquoise area, and III and IV the red area. The relationships between the two pairs are  $\Sigma 3$ , or close to this. Grains with other Euler angle values were present in this data set, but these had very low image quality values, and were therefore not investigated.

While it is not possible to draw general conclusions from data on such small areas, these results do agree with the observations of Gourgues *et al.* (2000) of the frequent occurrence of near- $\Sigma 3$  relationships. A suggestion of the possible arrangements of structural components is given in Figure 7.34.

No.	$\phi_1$	$\Phi$	$\phi_2$	Area / $\mu\text{m}^2$
I	64.3	39.2	338.8	123.2
II	214.2	48.5	114.4	10.6
III	291.3	5.3	69.8	7.9
IV	335.8	8.7	32.1	5.1

Table 7.3: Orientation components found in AQ sample.

Pair		Relationship	Brandon's ratio
I	II	$\Sigma 1$	0.56
I	III	$\Sigma 3$	0.75
I	IV	Random, near $\Sigma 3$	1.21 from $\Sigma 3$
II	III	$\Sigma 3$	0.72
II	IV	$\Sigma 3$	0.90
III	IV	$\Sigma 1$	0.60

Table 7.4: Relationships between different orientations in as-quenched sample.

## 7.10 Relationship to magnetic properties

In the  $2\frac{1}{4}\text{Cr1Mo}$  samples of Moorthy *et al.* (1997b, 1998, 2000), recrystallisation began to occur after prolonged tempering at  $650^\circ\text{C}$ . In this study, however, there was no recrystallisation. The clear lath structure in the AQ sample disappeared during tempering, but orientation relationships between microstructural components appeared to remain constant. The most obvious change was the reduction in strain evident from the increase in image quality.

The effect of such a structure on magnetic properties depends on whether domain walls interact more strongly with strain, or with the magnetostatic energy arising from misorientations at grain boundaries.

If strain is more important, domain walls in the AQ sample will undergo a large number of pinning and unpinning events, with a short mean free path. Within a single variant, if the domain walls are oriented parallel to the lath lengths, the mean free path will be of the order of the lath width. After tempering, the interlath strain energy decreases and the laths coalesce into a continuum with slight orientation variations. This would allow easier

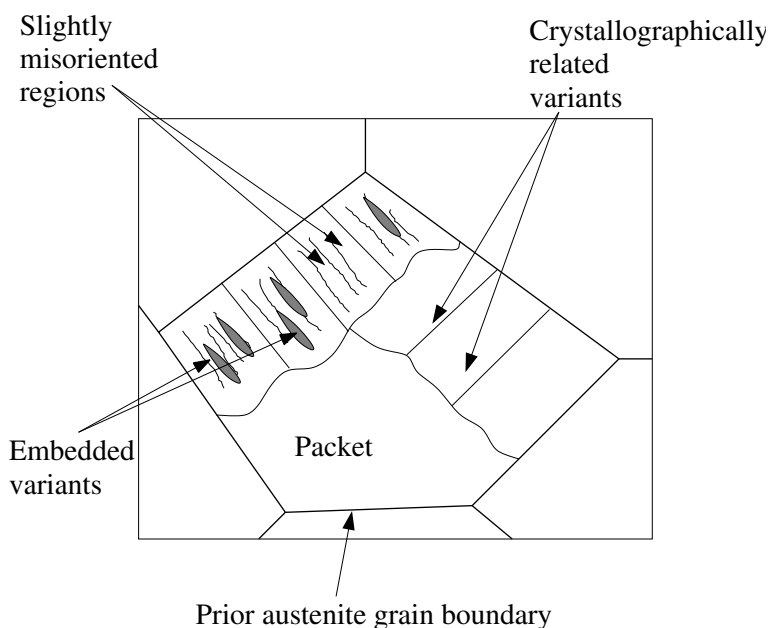


Figure 7.34: Possible levels of structure in 2.25Cr1Mo wt. % martensite, as deduced from OIM observation.

passage for domain walls; the main obstacles to their motion would be block, packet and prior austenite grain boundaries. However, tempering also causes the precipitation of carbides, which pin domain walls. In these samples, the strain reduction appears to be gradual rather than sudden, so the changes in BN peak shape and position may be rather smaller than those observed by Moorthy *et al.*

If, instead, misorientations are more important in domain wall pinning, there would be very little difference between the behaviour of domain walls in the AQ and tempered samples apart, perhaps, from the effect of carbides.

## 7.11 Conclusions

OIM observations of as-quenched and tempered  $2\frac{1}{4}$ Cr1Mo have been made. The most pronounced effects of tempering were a reduction in the lattice strain, and an increase in the number of points from which a diffraction pattern can be indexed with confidence by the software. This was attributed

to a decrease in strain due to a reduction in dislocation density at grain and lath boundaries.

Prior austenite grain boundaries were always random, and within the prior austenite grains a combination of low-angle,  $\Sigma 3$  and random boundaries occurred. Individual crystallographic packets contained many slightly misoriented groups of laths. Variants related by  $\Sigma 3$  were found; in some cases one variant was found in small regions embedded in large areas of another variant.

An estimation of the likely effect of these tempered microstructures on BN has been made, and will be tested in Chapter 8.